Check for updates

AGU ADVANCING EARTH AND SPACE SCIENCES

Water Resources Research

RESEARCH ARTICLE
10.1029/2024WR039718

Coupled Hydrologic and Biogeochemical Responses of Nitrate Export in a Tile-Drained Agricultural Watershed Revealed by SAS Functions and Nitrate Isotopes

Minghui Sha[1], Zhongjie Yu[1], Paolo Benettin[2], Lowell E. Gentry[1], and Corey A. Mitchell[1]

[1]Department of Natural Resources and Environmental Sciences, University of Illinois at Urbana-Champaign, Urbana, IL, USA, [2]Institute of Earth Surface Dynamics, Université de Lausanne, Lausanne, Switzerland

Key Points:

- Interactions between flow path variations and subsurface nitrogen cycling drive seasonally variable nitrate export regimes
- Interannual nitrate chemostasis is controlled by coupled responses of nitrogen cycling and hydrologic transport to wetness conditions
- Integrating water age and nitrate isotopes can reveal macroscale mechanisms driving watershed-scale nitrogen reactive transport

Supporting Information:

Supporting Information may be found in the online version of this article.

Correspondence to:

Z. Yu,
zjyu@illinois.edu

Citation:

Sha, M., Yu, Z., Benettin, P., Gentry, L. E., & Mitchell, C. A. (2025). Coupled hydrologic and biogeochemical responses of nitrate export in a tile-drained agricultural watershed revealed by SAS functions and nitrate isotopes. *Water Resources Research*, *61*, e2024WR039718. https://doi.org/10.1029/2024WR039718

Received 15 DEC 2024
Accepted 19 SEP 2025

Author Contributions:

Conceptualization: Zhongjie Yu
Data curation: Minghui Sha, Zhongjie Yu, Lowell E. Gentry, Corey A. Mitchell
Formal analysis: Minghui Sha, Zhongjie Yu
Funding acquisition: Zhongjie Yu
Investigation: Minghui Sha, Zhongjie Yu
Methodology: Zhongjie Yu, Paolo Benettin
Project administration: Zhongjie Yu, Lowell E. Gentry, Corey A. Mitchell
Resources: Zhongjie Yu, Lowell E. Gentry
Software: Paolo Benettin

© 2025. The Author(s).
This is an open access article under the terms of the Creative Commons Attribution License, which permits use, distribution and reproduction in any medium, provided the original work is properly cited.

Abstract The combination of high nitrogen (N) inputs on tile-drained agricultural watersheds contributes to excessive nitrate (NO_3^-) loss to surface- and groundwater systems. This study combined water age modeling based on StorAge Selection functions and NO_3^- isotopic analysis to examine the underlying mechanisms driving NO_3^- export in an intensively tile-drained mesoscale watershed typical of the U.S. Upper Midwest. The water age modeling revealed a pronounced inverse storage effect and strong young water preference under high-flow conditions, emphasizing evolving water mixing behavior driven by groundwater fluctuation and tile drain activation. Integrating NO_3^- concentration-isotope-discharge relationships with water age dynamics disentangled the interactions between flow path variations and subsurface N cycling in shaping seasonally variable NO_3^- export regimes at the watershed scale. Based on these results, a simple transit time-based and isotope-aided NO_3^- transport model was developed to estimate the timescales of watershed-scale NO_3^- reactive transport. Model results demonstrated variable NO_3^- source availability and a wetness dependence for denitrification, indicating that interannual NO_3^- chemostasis is driven by coupled and proportional responses of soil NO_3^- production, denitrification, and flow path activation to varying antecedent wetness conditions. These findings suggest that intensively tile-drained Midwestern agricultural watersheds function as both N transporters and transformers and may respond to large-scale mitigation efforts within a relatively short timeframe. Collectively, the results of this study demonstrate the potential of integrated water age modeling and NO_3^- isotopic analysis to advance the understanding of macroscale principles governing coupled watershed hydrologic and N biogeochemical functions.

Plain Language Summary Excessive nitrogen loss from agricultural watersheds with belowground drainage systems is a significant environmental concern. The relationship between discharge and nitrate (NO_3^-) concentrations measured at a watershed outlet provides insight into how the watershed stores, transforms, and releases nitrogen. However, this information is often inconclusive, as numerous factors drive variations in discharge and NO_3^- concentrations, making it difficult to identify the key mechanisms controlling their relationship. This study combined two useful metrics to better understand watershed NO_3^- concentration-discharge relationships: the age of water and the isotopic composition of NO_3^- in discharge. This approach is unique in that water age can be used to infer how water travels belowground to become discharge, while NO_3^- isotopes offer insights into microbial reactions that produce, transform, and consume NO_3^- within watersheds. The results show that NO_3^- concentration-discharge relationships, both seasonal and year-to-year, are controlled by simultaneous changes in water traveling paths and microbial nitrogen cycling, and that these changes are largely determined by how wet the watershed is in a given season or year. These findings have important implications for potential strategies to reduce nitrogen loss from artificially drained agricultural watersheds and for understanding how long it may take to observe mitigation outcomes.

1. Introduction

Agricultural intensification during the twentieth century significantly increased global soil nitrogen (N) surpluses from 20 to 138 Tg y^{-1} (Bouwman et al., 2013). As reactive N from large anthropogenic inputs cascades through the environment, numerous unintended consequences arise, including degraded water quality and biodiversity loss (Schulte-Uebbing et al., 2022). In the U.S. Midwest, approximately 40% of agricultural lands are currently drained by perforated pipes (tiles) buried belowground to enhance soil drainage (Valayamkunnath et al., 2020). The installation of these drainage systems has profoundly altered regional hydrologic and biogeochemical

Supervision: Zhongjie Yu
Validation: Minghui Sha, Zhongjie Yu
Visualization: Minghui Sha
Writing – original draft: Minghui Sha, Zhongjie Yu
Writing – review & editing: Minghui Sha, Zhongjie Yu, Paolo Benettin, Lowell E. Gentry, Corey A. Mitchell

regimes by "short-circuiting" subsurface structures, facilitating a substantial loss of nitrate (NO_3^-) to aquatic systems (Blann et al., 2009). Globally, subsurface artificial drains are widespread in lowland agricultural watersheds with poorly drained soils, leading to significant environmental concerns related to excessive N loss (Brauer et al., 2014; Rozemeijer et al., 2010).

1.1. Integration of NO_3^- C-Q Relationship, Isotope Biogeochemistry, and Water Age

To manage N in the environment, an in-depth understanding of how hydrologic, biogeochemical, and anthropogenic drivers interact to control NO_3^- export is needed. Solute concentration-discharge (C-Q) relationships observed at a watershed outlet are widely used as a top-down constraint for understanding watershed hydrologic and biogeochemical behaviors. In tile-drained and intensively managed agricultural watersheds, annual NO_3^- loads often scale linearly with discharge (Bauwe et al., 2020; Danalatos et al., 2022; Gentry et al., 2014), indicating a nearly invariant mean annual NO_3^- concentration after accounting for flow variations. This biogeochemically stationary export regime, known as "chemostasis" (Godsey et al., 2009), implies the presence of a large and spatially homogeneous N mass store resulting from the accumulation of legacy N in soil and groundwater systems (Basu, Destouni, et al., 2010; Thompson et al., 2011). However, the detailed mechanisms governing the sources and dynamics of this legacy N store are not fully understood (Basu et al., 2022).

At seasonal and event scales, NO_3^- concentration responses to fluctuations in discharge can be highly variable, depending on hydrogeological settings, external N inputs, and antecedent wetness conditions (Knapp et al., 2022; Musolff et al., 2015; Zhi & Li, 2020; Zimmer et al., 2019). This variability is attributed to the interactions between flow generation and NO_3^- source mobilization, along with the characteristic distribution of NO_3^- source zones, both vertically along the soil profile and laterally across the hillslope catena (Basu, Destouni, et al., 2010; Godsey et al., 2009; Seibert et al., 2009). However, current theories and empirical interpretations of NO_3^- export regimes often do not address underlying biogeochemical processes that co-occur with hydrologic variations. Soil N cycling is controlled by variations in temperature and soil moisture (Davidson & Janssens, 2006). Since these factors can covary with watershed storage and hydrologic regimes, concurrent variations in hydrologic connectivity and biogeochemical reactivity can confound the attribution of dominant processes driving emergent C-Q relationships. This interplay may be particularly important in agricultural watersheds, where fertilization and crop planting/harvesting cycles often synchronize with the seasonality of thermal and hydrologic regimes.

In this context, NO_3^- isotope analysis emerges as a promising tool for disentangling the relative contributions of watershed-scale biogeochemical processes to variability in NO_3^- C-Q relationships. The natural abundance isotope ratios of $^{15}N/^{14}N$ and $^{18}O/^{16}O$ in NO_3^- (denoted as $\delta^{15}N$ and $\delta^{18}O$) are intrinsic tracers of biogeochemical NO_3^- transformations due to the distinct isotope fractionations that occur during enzyme-driven N cycling reactions (Granger & Wankel, 2016; Kendall et al., 2007). For example, the process of nitrification (i.e., aerobic oxidation of ammonia to NO_3^-) not only increases NO_3^- concentration but also imprint a characteristic low $\delta^{18}O$ signature on produced NO_3^-, reflecting the $\delta^{18}O$ values of the oxygen substrates (i.e., H_2O and O_2), as well as the oxygen isotope fractionations during nitrification (Boshers et al., 2019; Hu et al., 2024). Similarly, while soil microbial NO_3^- assimilation has been shown to minimally alter $\delta^{15}N$ and $\delta^{18}O$ values (Fang et al., 2015), denitrification—the anaerobic reduction of NO_3^- to N_2—induces strong isotope fractionations, leading to a marked and coupled increase in the $\delta^{15}N$ and $\delta^{18}O$ values of the remaining NO_3^- (Granger et al., 2008). Thus, the balance of nitrification and denitrification leaves an indelible signature on NO_3^- isotopes, which can be used to quantify the relative rates of these processes (Casciotti, 2016). Nevertheless, a major challenge in applying NO_3^- isotope fingerprinting to watershed systems lies in untangling the combined effects of water mixing and NO_3^- transformation on observed isotope signatures. As water of different origins and ages carries NO_3^- with distinct transformation histories and, consequently, varying degrees of isotope fractionation, the mixing of these waters during flow generation can obscure the functional relationship between NO_3^- isotope variability and its underlying biogeochemical drivers at the watershed scale (Druhan & Maher, 2017).

Notably, recent advances related to quantifying time-variant water transit times have significantly improved our understanding of storage, flow paths, and sources of water in various hydrologic systems (Benettin et al., 2022; Rinaldo et al., 2015). The development of StorAge Selection (SAS) functions has provided a theoretical framework that links water transit time with water residence time in storage, thus enabling new investigations into storage-dependent flow generation processes (Botter et al., 2011; Harman, 2015; van der Velde et al., 2012). Applying these functions to heterogeneous watershed systems represents a practical advance, as they effectively

19447973, 2025, 10, Downloaded from https://agupubs.onlinelibrary.wiley.com/doi/10.1029/2024WR039718 by Readcube (Labtiva Inc.), Wiley Online Library on [28/10/2025]. See the Terms and Conditions (https://onlinelibrary.wiley.com/terms-and-conditions) on Wiley Online Library for rules of use; OA articles are governed by the applicable Creative Commons License

19447973, 2025, 10, Downloaded from https://agupubs.onlinelibrary.wiley.com/doi/10.1029/2024WR039718 by Readcube (Labtiva Inc.), Wiley Online Library on [28/10/2025]. See the Terms and Conditions (https://onlinelibrary.wiley.com/terms-and-conditions) on Wiley Online Library for rules of use; OA articles are governed by the applicable Creative Commons License

reduce complex three-dimensional transport dynamics into a single, time-variant water age distribution (Benettin et al., 2022). Previous studies have demonstrated strong correlations between time-variant water age and NO_3^- export at the watershed scale, highlighting water age as an intrinsic measure of subsurface N transport and reaction timescales (Benettin et al., 2020; Kaandorp et al., 2021; van der Velde et al., 2012; Yang et al., 2018). However, moving beyond these correlations to quantify the rates of biogeochemical processes using the SAS framework is challenging, as it requires explicit formulations to describe how NO_3^- is produced and removed over the residence time of its carrier water (Li et al., 2021).

Therefore, given their respective strengths and weaknesses, integrating NO_3^- C-Q relationship, NO_3^- isotopic analysis, and time-variant water age may shed new light on how watershed NO_3^- export regimes are shaped by co-occurring hydrologic and biogeochemical processes. In particular, confronting observed variations in NO_3^- C-Q relationships and isotopic signatures with time-variant water age distributions may not only reveal how NO_3^- is stored and distributed across subsurface layers (e.g., shallow vs. deep or hillslope vs. riparian), but also identify the dominant N sources and biogeochemical processes (e.g., relative rates of nitrification and denitrification) contributing to this heterogeneity. When examined across temporal scales, this approach may provide new insights into the co-evolution of subsurface hydrologic and biogeochemical processes under varying antecedent conditions, ultimately supporting a robust formulation that links water age to subsurface N transformation to constrain watershed-scale NO_3^- reactive transport.

1.2. Initial Integration and Objectives of This Study

Our previous study has pioneered the integration of NO_3^- C-Q relationships, NO_3^- isotopes, and time-variant water age at the scale of individual tile-drain outlets (Yu et al., 2023). We found that although NO_3^- concentrations in tile drainage varied limitedly over a wide range of discharge, both water age and NO_3^- isotope ratios consistently declined with increasing tile flow. These patterns suggest evolving hydrologic connectivity and vertical gradients in biogeochemical cycling between the surface soil and tile drains, modulated by antecedent wetness conditions. Building on these results, we developed a simple NO_3^- transport model using a Lagrangian formulation based on water age and incorporating isotope fractionation during subsurface NO_3^- reactive transport. This integrated approach successfully reproduced the chemostatic export behavior of NO_3^- and its isotope dynamics in tile drainage, highlighting coupled hydrologic and biogeochemical responses in driving NO_3^- export. It is important to note that this prior work assumed constant NO_3^- source availability and steady denitrification kinetics to reflect relatively stable field conditions over a 6-month period without fertilizer N input. To our knowledge, C-Q relationships, NO_3^- isotopes, and time-variant water age have not been examined side by side at the watershed scale to explore their combined potential.

In this study, we integrate (a) multi-year measurements of NO_3^- concentrations and isotopes, (b) water age estimates derived from a unique 30-year chloride (Cl^-) tracer record, and (c) a parsimonious modeling approach to investigate the mechanisms controlling NO_3^- export regimes in an intensively tile-drained, mesoscale agricultural watershed in east-central Illinois, USA. We begin by analyzing simultaneous variations in discharge, NO_3^- concentration, and isotopic signatures to identify emergent or persistent patterns. These patterns are then interpreted in the context of storage-dependent flow path variability, as inferred from SAS-based water age estimates across seasonal to interannual scales. Identified presence or absence of couplings is subsequently used to inform the calibration of the NO_3^- transport model adapted from Yu et al. (2023). Importantly, to address the added complexity of watershed-scale processes over multi-year periods, the NO_3^- transport model was extended to account for potentially different flow generation mechanisms in hillslope versus riparian areas, as well as variable NO_3^- source availability and denitrification along subsurface transport. Results are discussed in the context of N loss and legacy effects in intensively managed watersheds of the U.S. Upper Midwest. Specifically, this study addresses the following research questions:

1. How do water age, NO_3^- concentration, and NO_3^- isotopes vary with discharge, and what can that tell us about the coupling of watershed hydrologic and biogeochemical functions?
2. How do the biogeochemical processes driving NO_3^- export respond to changes in antecedent wetness conditions, and can we discern this response at the watershed scale?

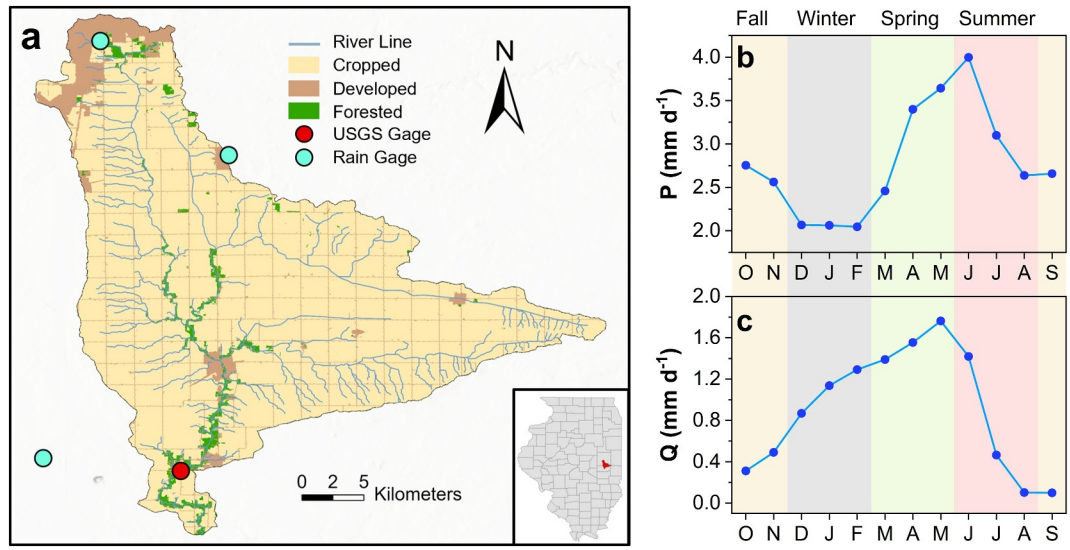

Figure 1. (a) Map showing the Upper Embarras River watershed. Water samples were collected near the USGS flow gage. Monthly average precipitation (b) and discharge (c) over the 30-year period. Monthly values are presented in the time sequence of a water year, defined as October through September of the following year. Shaded areas in panels (b, c) represent the four seasons.

2. Materials and Methods

2.1. Study Area

This study focuses on the 480 km^2 Upper Embarras River watershed (UER), located near Tuscola, Illinois (Figure 1a). This region has a humid continental climate, with cold winters (average January temperature of −2°C) and warm summers (average July temperature of 23°C). The mean annual precipitation for the period 1994–2023 was 1,010 mm. Approximately 10% of annual precipitation falls as snow during the winter, though snow accumulation rarely lasts longer than a few weeks, and often melts within a few days.

The UER is representative of the glaciated U.S. Upper Midwest, featuring low topography (i.e., surface slope <2%) and deep, poorly drained soil. The physiographic setting is the Bloomington Ridged Plain of the Till Plains Section, Central Lowland Province (Leighton et al., 1948). Surface materials of this region were mainly deposited during the Wisconsin Episode and consist of moderately thick loess (1–1.5 m) overlying glacial tills and lacustrine silts and clays (Mehnert et al., 2005). Bedrock of the Pennsylvanian age is generally 60–100 m below the surface (Soller et al., 1999). Soils in the UER are predominantly Mollisols formed in loess and the underlying glacial tills that originally supported prairie vegetation (Fehrenbacher, 1984). Drummer (fine-silty, mixed, superactive, mesic Typic Endoaquolls) silty clay loams and closely related soils (Flanagan-Catlin) are the dominant soil types in the watershed (USDA-NRCS, 2016).

The UER is predominantly agricultural, with row crop corn and soybean production covering 90% of the surface area. Due to the flat topography and poorly drained soils, the watershed is intensively tile-drained. According to David et al. (1997), about 80% of the watershed area is drained by parallel tile systems buried about 1 m below the surface. Moreover, the drainage network of the UER is dominated by straight, deep, trapezoidal ditches engineered to efficiently collect and convey tile outflow. These artificial channels have increased both drainage density and stream length by a factor of three compared to pre-settlement conditions (Rhoads et al., 2016). The widespread implementation of tile-and-ditch systems has profoundly altered the watershed's fluvial landscape, eliminating much of the natural riparian corridor and diminishing riparian-stream connectivity (Urban & Rhoads, 2003). As shown in Figure 1a, the remaining riparian zones are mostly restricted to the lower portion of the watershed and along the main stem.

19447973, 2025, 10, Downloaded from https://agupubs.onlinelibrary.wiley.com/doi/10.1029/2024WR039718 by Readcube (Labtiva Inc.), Wiley Online Library on [28/10/2025]. See the Terms and Conditions (https://onlinelibrary.wiley.com/terms-and-conditions) on Wiley Online Library for rules of use; OA articles are governed by the applicable Creative Commons License

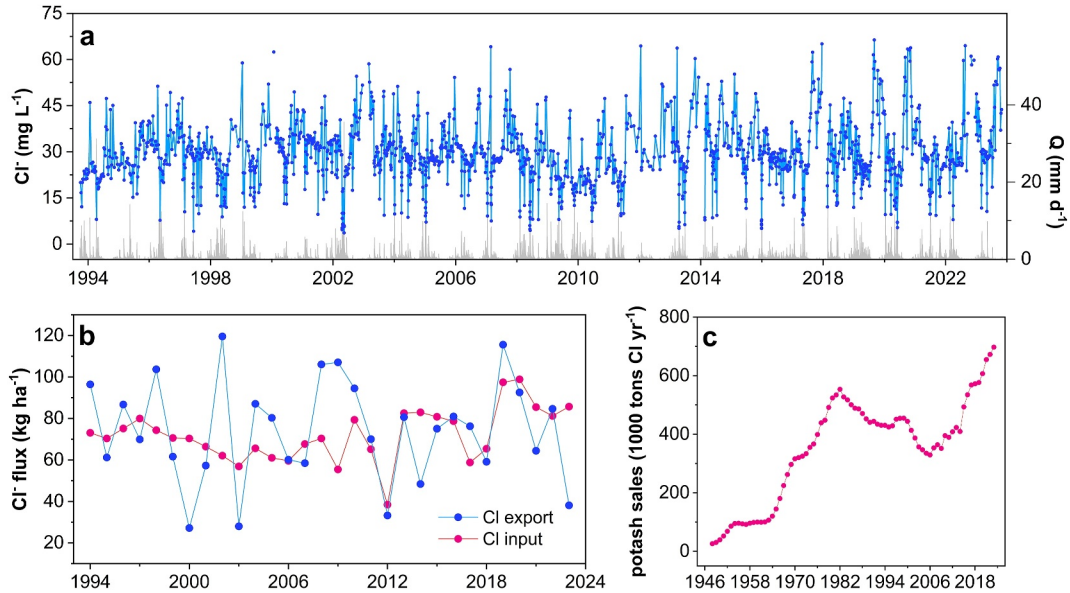

Figure 2. (a) Cl concentrations measured at the UER watershed outlet from 1994 to 2023. Also shown is daily discharge to aid interpretation. (b) Comparison of annual Cl input and export fluxes. (c) Long-term record of potash (KCl) sales in Illinois.

2.2. Data

2.2.1. Meteorological and Discharge Data

Long-term, continuous precipitation and meteorological data are available from three weather stations located within or near the UER watershed (Figure 1a). For this study, we calculated annual quantities based on the water year, defined as October to the following September, as it better aligns with the flow regime in this region. Therefore, the seasonality of a water year follows the sequence of fall (September, October, November), winter (December, January, February), spring (March, April, May), and summer (June, July, August) (Figures 1b and 1c). A United States Geological Survey gaging station near the watershed outlet (39° 47′ 29″ N, 88° 11′ 08″ W, gage ID: 03343400) provides 15-min river discharge data (Figure 1a). Like many Midwestern agricultural watersheds, discharge in the UER exhibits strong seasonality, with high discharge typically occurring in the winter-spring season when most fields in the watersheds are left bare fellow (Figure 1c). During the summer-fall season, daily discharge is often low (i.e., <0.1 mm d^{-1}) and nonresponsive to precipitation events due to enhanced crop evapotranspiration (ET) and dry antecedent conditions (Figure 1c). However, significant interannual variations in discharge seasonality can occur, depending on the timing and magnitude of precipitation each year. Over the 30-year period from 1994 to 2023, the mean ratio of potential ET (calculated via the Penman-Monteith equation) to precipitation was 1.01, while the mean annual runoff ratio was 0.34. A Mann-Kendall trend test indicated no significant monotonic trend in annual precipitation or discharge over the 30-year period (Figure S1 in Supporting Information S1).

2.2.2. Cl^- Concentration Data and Input Fluxes

Water samples were collected at the watershed outlet, co-located with the USGS gaging station, between October 1994 and September 2023. The sampling program is based on weekly samples and more frequent sampling during some episodes, particularly large spring storm events. The collected samples were filtered and analyzed for Cl^- concentration using a Dionex ion chromatograph. Cl^- concentration data from 1994 to 2015 were previously reported by David et al. (2016) to investigate watershed-scale Cl^- export and mass balance.

In this study, we used the entire 30-year data set to model the water age of discharge under a wide range of external forcing intensities. Observed Cl^- concentrations were highly sensitive to changes in hydrologic regimes, with large and often sporadic declines in concentration observed during winter and spring storm events (Figure 2a). On the other hand, significantly elevated concentrations (e.g., >50 mg L^{-1}) were typical during the summer-fall season (Figure 2a). This behavior is typical of Cl^- in human-impacted watersheds, where

19447973, 2025, 10, Downloaded from https://agupubs.onlinelibrary.wiley.com/doi/10.1029/2024WR039718 by Readcube (Labtiva Inc.), Wiley Online Library on [28/10/2025]. See the Terms and Conditions (https://onlinelibrary.wiley.com/terms-and-conditions) on Wiley Online Library for rules of use; OA articles are governed by the applicable Creative Commons License

19447973, 2025, 10, Downloaded from https://agupubs.onlinelibrary.wiley.com/doi/10.1029/2024WR039718 by Readcube (Labtiva Inc.), Wiley Online Library on [28/10/2025]. See the Terms and Conditions (https://onlinelibrary.wiley.com/terms-and-conditions) on Wiley Online Library for rules of use; OA articles are governed by the applicable Creative Commons License

precipitation has lower Cl^- concentrations than soil water due to large anthropogenic Cl^- inputs (van der Velde et al., 2010). We calculated the annual flow-weighted mean concentration (FWMC) of Cl^- as: $\text{FWMC} = \sum_{i=1}^{n} Q_i C_i / \sum_{i=1}^{n} Q_i$, where Q_i is daily discharge and C_i is the linearly interpolated daily Cl^- concentration from measured values (Williams et al., 2015). The FWMC of Cl^- varied between 17.8 mg L^{-1} and 30.5 mg L^{-1} during the study period and did not exhibit a significant monotonic trend (Mann-Kendell test, $P > 0.05$) (Figure S1 in Supporting Information S1). This absence of a significant trend is similar to observations in the intensively agricultural Kervidy-Naizin watershed in western France (Aubert et al., 2014) but is very different from those at other sites, where reductions in Cl^- input loads have resulted in declining stream Cl^- concentrations (e.g., Kaandorp et al. (2021)).

David et al. (2016) provided a detailed estimate of annual Cl^- input via Cl^- fertilizers and road salts in the UER from 1994 to 2014. A description of the estimation method can be found in Text S1 of Supporting Information S1. Using a similar method, we extended the input record to cover 2015 to 2023. The estimated annual total Cl^- input varied between 38.5 kg ha^{-1} yr^{-1} and 98.9 kg ha^{-1} yr^{-1} and was more variable after 2011 (Figure 2b), although the cause of this variability is unclear. On average, the annual Cl^- input was estimated to be 71.2 kg ha^{-1} yr^{-1} for the 30-year period. This average annual input is in close agreement with the average annual river export of 74.2 kg ha^{-1} yr^{-1}, suggesting a nearly balanced Cl^- input-output relationship over the study period. Furthermore, David et al. (2016) estimated a long-term trajectory of fertilizer Cl^- input for the state of Illinois using statewide fertilizer sales records. Extending this trajectory to the more recent years shows that substantial Cl^- fertilizer input did not occur in Illinois until around 1970 (Figure 2c) (Text S1 in Supporting Information S1).

2.2.3. NO_3^- Concentrations and Isotopes

We measured water samples collected between October 2020 and September 2023 for NO_3^- concentrations and isotopes ($n = 164$). NO_3^- concentrations were measured using the same ion chromatograph, with a detection limit of 0.1 mg N L^{-1}. For numerical convenience, samples below the detection limit were assigned a value of 0.1 mg N L^{-1}. NO_3^- isotopes were measured using the denitrifier method (Weigand et al., 2016) and an Elementar precisION isotope ratio mass spectrometer (Yu et al., 2023). The precision was ±0.1‰ for $\delta^{15}N$ and ±0.2‰ for $\delta^{18}O$. Since NO_3^- isotopic analysis requires only a small amount of NO_3^- (in our case, 20 nmol), all collected samples, including those below the concentration detection limit, were measured for NO_3^- isotopes. Note that NO_3^- concentration data from 1994 to 2020 are also available (Figure S2a in Supporting Information S1); some of them have been used in previous studies to derive watershed N mass balances (David et al., 2010; Gentry et al., 2014). Here, we primarily focus on the 3-year period from 2021 to 2023, for which we have isotope data, to explore how combining C-Q relationships, NO_3^- isotopes, and water age can improve our understanding of watershed-scale N reactive transport.

We calculated the FWMC of NO_3^- for the three study years using the same linear interpolation method as for Cl^-. Similarly, the annual load-weighted mean values (LWMV) of $\delta^{15}N$ and $\delta^{18}O$ were estimated by linearly interpolating measured isotope values on a daily scale. Following previous studies in this region (Ma et al., 2023; Marinos et al., 2020), we used a piecewise power law relationship to characterize NO_3^- export regimes in the UER:

$$C_{NO3} = \begin{cases} aQ^{b_1} & Q < Q_t \\ aQ_t^{b_2-b_1}Q^{b_2} & Q \geq Q_t \end{cases} \quad (1)$$

where a, b_1, b_2, and the threshold discharge Q_t are fitted parameters using iterative least squares estimation. In the absence of prior knowledge, both linear and power law relationships—applied to all data or in a piecewise fashion—were used to examine the relationships between measured NO_3^- isotopes and discharge.

2.2.4. N Source Inputs and Annual Surplus

To contextualize measured NO_3^- concentrations, loads, and isotopes, we retrieved annual N source inputs and N surplus (i.e., the difference between annual N inputs and crop N uptake) for Champaign and Douglas Counties, where the UER is located, from the TREND-Nitrogen database (Byrnes et al., 2020). These data are available for the period between 1930 and 2017. According to the TREND-Nitrogen database, synthetic fertilizer and soybean

biological N fixation dominated watershed N source inputs between 1994 and 2017 (combined, 175 kg N ha^{-1} yr^{-1}), accounting for 94% of annual total inputs, whereas other sources, including manure and atmospheric deposition (combined, 6.4 kg N ha^{-1} yr^{-1}) were largely negligible. During this period, N surplus ranged from 14.6 to 78.2 kg N ha^{-1} yr^{-1}, with an average of 41.4 kg N ha^{-1} yr^{-1} (Figure S2b in Supporting Information S1). A comparison between measured NO_3^- FWMC and N surplus from 1994 to 2017 reveals no clear hysteresis and lacks a statistically significant linear relationship ($P > 0.05$) (Figure S2c in Supporting Information S1).

2.3. Water Age Modeling

We used the *tran*-SAS software (Benettin & Bertuzzo, 2018a) to estimate storage and model the time-variant backward water age distribution of discharge. The model setup largely followed our previous work (Yu et al., 2023). Below, we summarize the basic model assumptions. A detailed description of the model structure, SAS function parameterization, numerical implementation, and calibration can be found in Text S2 of Supporting Information S1.

To describe watershed-scale water mixing and solute transport, the entire UER watershed was spatially lumped into a single control volume, with precipitation as the only water input and discharge and ET as the outflows. We estimated daily ET using the FAO approach, incorporating crop-specific growth information for the UER region. A rainfall-runoff model, based on a power law catchment sensitivity function described in Kirchner (2009), was then used to calibrate ET and estimate the daily watershed storage anomaly, ΔS, defined as the deviation in watershed storage relative to an arbitrary datum. We normalized ΔS by subtracting its estimated minimum value, so that after normalization, the minimum ΔS from 1994 to 2023 was zero. The calibrated daily ET fluxes and normalized ΔS, along with directly observed daily precipitation and discharge, were used as inputs to the water age model (i.e., following the direct or "pure" SAS approach; Benettin et al. (2022)).

By definition, the time-variant water age distribution of discharge, $p_Q(T,t)$, can be obtained by differentiating the SAS function of discharge with respect to water age (T). Subsequently, $p_Q(T,t)$ can be used to compute stream water Cl^- concentration, $C_Q(t)$, as follows:

$$C_Q(t) = \int_0^\infty C_S(T,t)\, p_Q(T,t)\, dT \tag{2}$$

where $C_S(T,t)$ is the Cl^- concentration of a water parcel of age T at time t in storage. The use of Equation 2 requires specification of the SAS functions of discharge and ET, as well as how $C_S(T,t)$ is linked to Cl^- source input and responds to potentially non-conservative Cl^- cycling processes. Given that precipitation in this area contains negligible Cl^- (<0.2 mg L^{-1}) (NADP, 2024), we assumed that $C_S(T,t)$ is determined by Cl^- inputs via fertilizers and road salts (Figure 2b). To introduce Cl^- into storage, the estimated annual Cl^- inputs were disaggregated into daily mass fluxes and subsequently distributed across estimated fertilizer and road salt application periods (Hrachowitz et al., 2015). We assumed that ET does not remove Cl^- from storage (i.e., complete evapoconcentration), consistent with our previous work in a nearby tile-drained corn-soybean field (Yu et al., 2023). This assumption is supported by the close balance between the estimated annual Cl^- input and river export (Figure 2b), as well as field evidence showing negligible Cl^- export via corn and soybean grain harvest (about 2.5 kg ha^{-1} yr^{-1}) relative to river export (Batal et al., 2011; David et al., 2016). Moreover, since ET accounted for two-thirds of annual precipitation during the study period, if ET were to significantly consume Cl^- from storage, a large subsurface legacy Cl^- store would be required to sustain river Cl^- export, which is unlikely given the low historical Cl^- input (Figure 2c).

We used a uniform function over the interval (0, u_{ET}] for the SAS function of ET, with $u_{ET} \in (0,1]$ defining the upper boundary of the fractional age-ranked storage from which ET draws water (Benettin et al., 2020). A power law function was used to parameterize the SAS function of discharge. The power-law shape exponent k controls the outflow's affinity for younger or older water in storage: values of $k < 1$ indicate a preference for younger water, while $k > 1$ indicates a preference for older water. The further k deviates from 1, the stronger the preferential selection. In the special case where $k = 1$, outflows sample uniformly from storage, corresponding to complete mixing conditions. These water age selection behaviors have been linked to watershed-scale transport patterns within the advection-dispersion framework (see Text S2 in Supporting Information S1).

19447973, 2025, 10, Downloaded from https://agupubs.onlinelibrary.wiley.com/doi/10.1029/2024WR039718 by Readcube (Labtiva Inc.), Wiley Online Library on [28/10/2025]. See the Terms and Conditions (https://onlinelibrary.wiley.com/terms-and-conditions) on Wiley Online Library for rules of use; OA articles are governed by the applicable Creative Commons License

19447973, 2025, 10, Downloaded from https://agupubs.onlinelibrary.wiley.com/doi/10.1029/2024WR039718 by Readcube (Labtiva Inc.), Wiley Online Library on [28/10/2025]. See the Terms and Conditions (https://onlinelibrary.wiley.com/terms-and-conditions) on Wiley Online Library for rules of use; OA articles are governed by the applicable Creative Commons License

Table 1
Summary of the Calibration Parameters and Performance of Water Age Model

Symbol	Definition	Initial range	Optimal value	Behavioral range
$k_{QHS,dry}$	SAS parameter for Q_{HS}	0.1–10[a]	0.12	0.10–0.19
$k_{QHS,wet}$	SAS parameter for Q_{HS}	0.1–10[a]	1.48	1.11–3.16
k_{QRP}	SAS parameter for Q_{RP}	0.1–10[a]	2.78	1.17–9.69
u_{ET}	SAS parameter for ET	0.1–1	0.87	0.42–0.99
S_0	Initial storage (mm)	500–5,000	1151	520–2549
Model performance metric				
KGE_{Cl}				0.72–0.74

[a]Parameter values are drawn from log-transformed ranges.

Initially, we used a single time-variant power law function based on ΔS to parameterize the SAS function for discharge. However, preliminary model runs consistently underestimated the elevated Cl^- concentrations during low flow periods in the summer-fall season. During these periods, the drainage network may retract substantially, and only riparian areas along the main channels may remain connected and contribute flows (Knapp et al., 2022). The transport characteristics of these near-stream zones, particularly those along the downstream main stem (Figure 1a), may differ from those of the watershed as a whole, introducing nonlinearities in seasonal transport regimes. For these reasons, we adopted the composite SAS approach proposed by Rodriguez and Klaus (2019) to express $Q(t)$ and $p_Q(T,t)$ as functions of two constituent flow paths:

$$Q(t) = Q_{HS}(t) + Q_{RP}(t) \tag{3}$$

$$p_Q(T,t) = \frac{Q_{HS}(t)}{Q(t)} p_{QHS}(T,t) + \frac{Q_{RP}(t)}{Q(t)} p_{QRP}(T,t) \tag{4}$$

where $Q_{HS}(t)$ and $Q_{RP}(t)$ are flows draining the hillslope and riparian areas, respectively; and $p_{QHS}(T,t)$ and $p_{QRP}(T,t)$ are the time-variant water age distributions of these two flow paths. Note that hillslope flow is defined generically here to represent an ensemble of flow paths activated during high flow periods, including tile drainage. To reduce the number of model parameters, we set $Q_{RP}(t)$ to be the lower fifth percentile of discharge measured during the 30-year period (i.e., 0.01 mm d^{-1}) or $Q(t)$, whichever is lower at each model timestep. Thus, $Q_{HS}(t) = Q(t) – Q_{RP}(t)$. This ensures that the influence of riparian areas is predominant during the driest periods but quickly diminishes as the watershed becomes wetter. We defined the SAS function for Q_{RP} as a time-invariant power law function with the exponent k_{RP}. A time-variant power law function was used for the SAS function of Q_{HS}, with the exponent varying between two extremes, $k_{HS,wet}$ and $k_{HS,dry}$, as a function of ΔS (Benettin et al., 2017; Yu et al., 2023).

To initialize the water age model, the total water storage at the beginning of the simulation, S_0, is needed. This results in five model calibration parameters (S_0, u_{ET}, k_{RP}, $k_{HS,wet}$, and $k_{HS,dry}$). Plausible uniform parameter ranges were estimated from our previous field-scale study (Yu et al., 2023) and from the literature (Benettin et al., 2020), as shown in Table 1. The model was ran 400,000 times using a standard Monte Carlo approach to sample parameter sets. Similar to previous studies focused on the linkage between water age and water quality (e.g., van der Velde et al. (2010)), we used all Cl^- data for model calibration without separating them into calibration and validation periods, as our goal is to integrate water age, C-Q relationships, and NO_3^- isotopes to better understand NO_3^- reactive transport. Model performance was evaluated based on the Kling-Gupta Efficiency criterion for simulated Cl^- concentrations (KGE_{Cl}). We retained the top-performing 100 parameter sets as behavioral, with the top-ranked set designated as optimal. We retrieved the median water age of daily discharge as a summary statistic from behavioral model simulations. Previous studies have shown that median water age is less impacted by uncertainties in old water contributions compared to mean water age (Benettin et al., 2017).

19447973, 2025, 10, Downloaded from https://agupubs.onlinelibrary.wiley.com/doi/10.1029/2024WR039718 by Readcube (Labtiva Inc.), Wiley Online Library on [28/10/2025]. See the Terms and Conditions (https://onlinelibrary.wiley.com/terms-and-conditions) on Wiley Online Library for rules of use; OA articles are governed by the applicable Creative Commons License

2.4. NO_3^- Transport Modeling

2.4.1. Model Overview

The water age-based, isotope-aided NO_3^- transport model, originally proposed by van der Velde et al. (2010, 2012) and further developed in Yu et al. (2023), was modified to simulate both NO_3^- concentrations and isotopes at the watershed scale. Detailed information on the model framework is provided in Text S3 of Supporting Information S1. Briefly, the concentration of NO_3^- in discharge (C_{NO3}) is modeled using a Lagrangian description of NO_3^- reactive transport in the domain of water age distributions. Under this framework, subsurface heterogeneity along flow paths is encapsulated in the distribution of water ages, without explicitly tracking the spatial trajectory of individual water parcels (Botter et al., 2005; Rinaldo et al., 2006; van der Velde et al., 2012). Thus, following the arrival of an initially NO_3^--free water parcel as precipitation, the water parcel gradually acquires NO_3^- via mass transfer from immobile soil source zones. This mobile-immobile mass transfer is governed by a limiting concentration, C_{lim} (mg N L^{-1}), which is a lumped parameter representing source zone NO_3^- availability, as jointly controlled by external N inputs, biogeochemical cycling, and variations in soil water storage. The timescale of this transfer is controlled by an effective first-order kinetic constant, r_d (d^{-1}). Simultaneously, NO_3^- in mobile water parcels is subject to denitrification throughout its residence time in the watershed, governed by a first-order rate constant, r_n (d^{-1}). The resulting C_{NO3} at time t is obtained by convolving the water age distribution with the NO_3^- age-response function (van der Velde et al., 2012):

$$C_{NO3}(t) = \int_0^\infty C_{lim}\left(1 - e^{-r_d T}\right) e^{-r_n T} p_Q(T,t)\, dT \tag{5}$$

Although this Lagrangian formulation is spatially lumped, Equation 5 is conceptually analogous to a two-storage model comprising a root zone and groundwater compartment, with r_d and r_n defining the characteristic timescales of NO_3^- mass transfer and denitrification, respectively (Text S3; Figure S14 in Supporting Information S1). Additionally, Equation 5 assumes that there is no spatial gradient in C_{lim} and that longitudinal mixing between water parcels can be neglected, so that transport becomes convective through independent streamlines. Both assumptions may be valid in agricultural watersheds with dense drainage networks and large diffuse NO_3^- inputs (Botter et al., 2005; Loschko et al., 2016).

Previous use of Equation 5 focused on relatively short periods during which C_{lim} was assumed constant (van der Velde et al., 2012; Yu et al., 2023). However, at the seasonal scale, C_{lim} is expected to vary significantly due to fertilizer applications and biogeochemical cycling. To incorporate this variability, Equation 5 is reformulated as:

$$C_{NO3}(t) = \int_0^\infty C_{lim}(t-T)\left(1 - e^{-r_d T}\right) e^{-r_n T} p_Q(T,t)\, dT \tag{6}$$

This revised formulation accounts for the fact that C_{lim} depends on the biogeochemical conditions at the time each water parcel entered the system. Consequently, watershed-scale NO_3^- export integrates the full history of hydrologic and biogeochemical interactions.

To simulate the $\delta^{18}O$ values of NO_3^- in discharge, Equation 6 was extended to track the concentrations of NO_3^- isotopologues (Yu et al., 2023):

$${}^{16}C_{NO3}(t) = \int_0^\infty {}^{16}C_{lim}(t-T)\left(1 - e^{-r_d T}\right) e^{-r_n T} p_Q(T,t)\, dT \tag{7}$$

$${}^{18}C_{NO3}(t) = \int_0^\infty {}^{18}C_{lim}(t-T)\left(1 - e^{-r_d T}\right) e^{-\left(r_n/{}^{18}\alpha\right)T} p_Q(T,t)\, dT \tag{8}$$

Here, ${}^{16}C_{NO3}$ and ${}^{18}C_{NO3}$ represent the concentrations of the major NO_3^- isotopologue $N^{16}O^{16}O^{16}O$ and the singly ^{18}O-substituted isotopologue $N^{18}O^{16}O^{16}O$, respectively (mg N L^{-1}); ${}^{16}C_{lim}$ and ${}^{18}C_{lim}$ are their corresponding limiting concentrations (mg N L^{-1}); and ${}^{18}\alpha$ is the kinetic oxygen isotope fractionation factor for denitrification (dimensionless). Because ${}^{18}\alpha > 1$, denitrification not only reduces the bulk concentration of NO_3^- but also simultaneously increases ${}^{18}C_{NO3}$ relative to ${}^{16}C_{NO3}$ (and thus $\delta^{18}O$) due to the slower rate of

19447973, 2025, 10, Downloaded from https://agupubs.onlinelibrary.wiley.com/doi/10.1029/2024WR039718 by Readcube (Labtiva Inc.), Wiley Online Library on [28/10/2025]. See the Terms and Conditions (https://onlinelibrary.wiley.com/terms-and-conditions) on Wiley Online Library for rules of use; OA articles are governed by the applicable Creative Commons License

denitrification for $N^{18}O^{16}O^{16}O$. This isotopologue modeling approach can also be used to simulate the $\delta^{15}N$ values of NO_3^-. However, we focused here on $\delta^{18}O$ due to its simpler source attribution (i.e., from O_2 and H_2O), avoiding the need to specify nitrogen isotopic signatures from distinct sources such as fertilizers, soil organic matter, or crop residues.

2.4.2. Model Specification

To maintain parsimony while still being able to resolve the dominant modes of hydrologic and biogeochemical processes driving NO_3^- export, several modeling decisions were made. First, given the lumped nature of the transport model, we focused on simulating NO_3^- concentrations and $\delta^{18}O$ in hillslope flow by using $p_{QHS}(T,t)$ from the water age modeling in Equations 6–8. To ensure closed N mass and isotope balances, we assumed a NO_3^- concentration of 0.1 mg N L^{-1} and a $\delta^{18}O$ value of 4.4‰—the median $\delta^{18}O$ value measured during low flow periods (i.e., <0.1 mm d^{-1})—for riparian flow, which matched the observations well.

Second, while C_{lim} could be potentially parameterized using a biogeochemical model that explicitly simulates NO_3^- production and consumption processes in the soil (e.g., Botter et al. (2008)), we adopted a simpler approach by assuming that C_{lim} varies seasonally but remains constant within each season for the entire time domain encompassed by the modeled backward water age distributions. In other words, each seasonal C_{lim} value is interannually invariant. This assumption resulted in four calibration parameters: one each for fall ($C_{lim,SON}$), winter ($C_{lim,DJF}$), spring ($C_{lim,MAM}$), and summer ($C_{lim,JJA}$).

Third, the use of Equations 7 and 8 requires specifying the $\delta^{18}O$ value of NO_3^- at the limiting condition, which can then be combined with the seasonal C_{lim} values to calculate $^{16}C_{lim}$ and $^{18}C_{lim}$. In practice, this $\delta^{18}O$ value can be construed as the $\delta^{18}O$ of NO_3^- resulting from nitrification (denoted as $\delta^{18}O_{nit}$) (Yu et al., 2023), the dominant NO_3^- production pathway in ammonia-fertilized agricultural soils. Because other NO_3^- consumption processes, aside from denitrification, exert minimal influence on NO_3^- isotopes (Fang et al., 2015), $\delta^{18}O$-NO_3^- in discharge largely reflects $\delta^{18}O_{nit}$ when denitrification is limited. Recent studies have shown that $\delta^{18}O_{nit}$ is mechanistically linked to the $\delta^{18}O$ of the water used in nitrification and can thus be predicted from $\delta^{18}O$-H_2O (Boshers et al., 2019; Hu et al., 2024). However, without knowledge of $\delta^{18}O$-H_2O at the watershed scale, we treated $\delta^{18}O_{nit}$ as a calibration parameter for the entire modeling period. This assumption of invariant $\delta^{18}O_{nit}$ will be discussed later.

We tested two different formulations of r_n to explore how hydrologic and biogeochemical interactions influence the timescales of denitrification at the watershed scale. The first formulation treats r_n as a constant, implying that the denitrification rate is insensitive to variations in watershed storage or hydrologic conditions. We refer to this configuration as the static model. In the second configuration, r_n is allowed to vary dynamically with watershed wetness. It is well established that denitrification rates increase under wetter soil conditions due to the development of anoxic reaction sites (Groffman et al., 2009). Additionally, wetter soil conditions may increase O_2 consumption via heterotrophic respiration, thereby promoting an earlier onset of denitrification in groundwater (Kolbe et al., 2019). To account for this wetness dependence of denitrification at the watershed scale, we modified r_n using a wetness scalar $\theta \in [0,1]$ based on ΔS (Kumar et al., 2020). Assuming a pulse of water enters the system at time t_i, θ is defined as a function of the average ΔS the parcel experienced while residing in the system ($\overline{\Delta S}$):

$$\theta(t_i+T)=\begin{cases}\left(\dfrac{\overline{\Delta S}(t_i+T)-S_r}{S_m-S_r}\right)^{\gamma} & \overline{\Delta S}(t_i+T)<S_r \\ 0 & S_r\le\overline{\Delta S}(t_i+T)\le S_m \\ 1 & \overline{\Delta S}(t_i+T)>S_m\end{cases} \tag{9}$$

$$\overline{\Delta S}(t_i+T)=\frac{1}{T}\int_{t_i}^{t_i+T}\Delta S(t')\,dt' \tag{10}$$

where S_m is the threshold $\overline{\Delta S}$ beyond which denitrification is assumed to be unlimited and proceeds with the maximum rate constant r_n for the entire time the parcel travels through the system (mm); S_r is the limit $\overline{\Delta S}$ below which denitrification is completely inhibited (mm); and γ is a shape factor defining the steepness of the relationship between θ and $\overline{\Delta S}$ when $\overline{\Delta S}$ falls in between S_r and S_m (dimensionless). Following previous work (Kumar

19447973, 2025, 10, Downloaded from https://agupubs.onlinelibrary.wiley.com/doi/10.1029/2024WR039718 by Readcube (Labtiva Inc.), Wiley Online Library on [28/10/2025]. See the Terms and Conditions (https://onlinelibrary.wiley.com/terms-and-conditions) on Wiley Online Library for rules of use; OA articles are governed by the applicable Creative Commons License

Table 2
Summary of the Calibration Parameters and Performance of the Dynamic NO_3^- Transport Model

Symbol	Definition	Initial range	Optimal value	Behavioral range
$C_{lim,SON}$	Fall limiting NO_3^- concentration (mg N L^{-1})	1–200	4.0	2.5–10.3
$C_{lim,DJF}$	Winter limiting NO_3^- concentration (mg N L^{-1})	1–200	12.3	8.4–41.5
$C_{lim,MAM}$	Spring limiting NO_3^- concentration (mg N L^{-1})	1–200	26.5	19.1–59.5
$C_{lim,JJA}$	Summer limiting NO_3^- concentration (mg N L^{-1})	1–200	5.5	1.1–5.6
r_d	First-order rate constant for NO_3^- mass transfer (d^{-1})	10^{-2}–10^{0}	0.31	0.070–0.69
r_n	First-order rate constant for denitrification (d^{-1})	10^{-5}–10^{0}	0.0037	0.0012–0.0040
$^{18}\alpha$	Oxygen isotope fractionation factor for denitrification (−)	1.000–1.040	1.019	1.010–1.038
$\delta^{18}O_{nit}$	$\delta^{18}O$ of nitrification-produced NO_3^- (‰)	−10–1	0.6	−0.8–0.8
S_m	Threshold storage for the wetness dependence of denitrification (mm)	1–208	123	106–138
Model performance metrics[a]				
KGE_{NO3}			0.78	0.70–0.78
$KGE_{\delta 18O}$			0.87	0.78–0.87

[a]Dates with NO_3^- concentration lower than 1 mg N L^{-1} were not included in the calculations of KGE_{NO3} and $KGE_{\delta 18O}$.

et al., 2020), we assumed that S_r is one-third of S_m and that $\gamma = 2.5$. Therefore, on any given day, the aggregated wetness effect on denitrification, θ_a, for hillslope flow can be described as:

$$\theta_a(t) = \int_0^{\infty} \theta(t-T)\, p_{QHS}(T,t)\, dT \tag{11}$$

We refer to this model with time-variant r_n as the dynamic model. Therefore, the static model has eight model parameters ($C_{lim,SON}$, $C_{lim,DJF}$, $C_{lim,MAM}$, $C_{lim,JJA}$, r_d, r_n, $^{18}\alpha$, and $\delta^{18}O_{nit}$), while the dynamic model has nine (all the parameters of the static model plus S_m).

2.4.3. Model Calibration

For both the static and dynamic models, we used the multicriteria optimization algorithm AMALGAM (Vrugt & Robinson, 2007) to calibrate the models and identify behavioral parameter sets. The KGE criteria for simulated NO_3^- concentration and $\delta^{18}O$ in discharge (KGE_{NO3} and $KGE_{\delta 18O}$) were used in AMALGAM as dual criteria to generate Pareto solutions—solutions that represent the best trade-off between KGE_{NO3} and $KGE_{\delta 18O}$. Importantly, the simulation of NO_3^- concentration and $\delta^{18}O$ in discharge is critically dependent on the water age distributions derived from the water age modeling, which are themselves uncertain. To incorporate this uncertainty, we retrieved transport parameter sets from behavioral water age simulations that correspond to the minimum, maximum, and every tenth percentile of flow-weighted mean median water age over the 30-year period. Each of these 11 transport parameter sets were used to drive the NO_3^- transport model and generate 100 Pareto solutions using AMALGAM. These Pareto solutions were combined for further identification of behavioral biogeochemical parameter sets.

Uniform parameter ranges for both the static and dynamic models are shown in Table 2. These ranges were designed to be as wide as possible while still being physically feasible. For example, the upper bound of the seasonal C_{lim} values was set to 200 mg N L^{-1}, which was derived from a typical fertilizer application rate to corn of 180 kg N ha^{-1}, an impacting soil depth of 30 cm, and a volumetric soil water content of 0.3 cm^3 cm^{-3}. Similarly, the upper bound of S_m was set to the maximum ΔS value estimated for 1994 to 2023 (i.e., 208 mm; see Text S2 in Supporting Information S1). The parameter ranges for $^{18}\alpha$ and $\delta^{18}O_{nit}$ were derived from recent synthesis of nitrification and denitrification isotope effects (Boshers et al., 2019; Denk et al., 2017). To minimize the impacts of riparian flow during low-flow periods, the calculations of KGE_{NO3} and $KGE_{\delta 18O}$ during model calibration were restricted to dates when NO_3^- concentrations were ≥1 mg N L^{-1}, during which over 99% of NO_3^- export occurred in each of the three study years.

19447973, 2025, 10, Downloaded from https://agupubs.onlinelibrary.wiley.com/doi/10.1029/2024WR039718 by Readcube (Labtiva Inc.), Wiley Online Library on [28/10/2025]. See the Terms and Conditions (https://onlinelibrary.wiley.com/terms-and-conditions) on Wiley Online Library for rules of use; OA articles are governed by the applicable Creative Commons License

We selected the most balanced solutions from the combined Pareto solution pool using the following criteria: $KGE_{NO3} \geq 0.7$ and $KGE_{\delta 18O} \geq 0.7$. To improve parameter identifiability, we also imposed a prior constraint that the modeled annual LWMV of $\delta^{18}O$ should have the same rank order as the observed values over the three study years. This constraint is based on the rationale that $\delta^{18}O$ reflects the watershed-scale NO_3^- biogeochemical cycling, and its annual variability provides a strong test of the model's ability to capture these dynamics. We designated parameter sets that simultaneously satisfied the KGE_{NO3} and $KGE_{\delta 18O}$ criteria and the prior constraint as behavioral. Among the behavioral parameter sets, the one with the highest average value of KGE_{NO3} and $KGE_{\delta 18O}$ was considered optimal.

2.4.4. Analysis

Using values of r_n from the behavioral model realizations, we estimated the denitrification timescale, RT_{50}, defined here as the time required for 50% removal of the initial NO_3^- (Kumar et al., 2020). We then calculated the dimensionless Damköhler number, Da_{50}, as the ratio of median water age to RT_{50}, to link hydrologic transport and denitrification timescales (Kumar et al., 2020). Additionally, by treating each behavioral model realization as an independent measure, we computed flow-weighted mean values of RT_{50} and Da_{50} for each of the three years. Interannual differences were then assessed using the non-parametric Friedman's test with Dunn-Sidàk correction for multiple comparisons.

3. Results

3.1. Relationships Between NO_3^- Concentrations, Isotopes, and Discharge

3.1.1. Temporal Dynamics of NO_3^- Concentrations and Isotopes

Measured NO_3^- concentrations and isotopes in discharge exhibited strong but opposing seasonal patterns over the 3-year period (Figure 3). NO_3^- concentrations typically increased from late winter to early spring each year, peaking around late spring to early summer (i.e., May and June), and then rapidly declined (Figure 3a). In contrast, $\delta^{15}N$ and $\delta^{18}O$ values were lowest during high-flow spring periods and increased during the summer-fall season when discharge began to decline but was not too low (Figures 3b and 3c). When plotting the measured $\delta^{15}N$ and $\delta^{18}O$ together, a coupled enrichment is evident along the gradient of decreasing NO_3^- concentrations, until NO_3^- concentrations fell below about 1 mg N L^{-1} (Figure 4). This coupled variation underscores denitrification as an important control on the temporal variability of $\delta^{15}N$ and $\delta^{18}O$ in discharge. Moreover, it suggests that once this coupled enrichment is corrected for, the exported NO_3^- maintained a consistent isotopic signature throughout most of the year, except during the driest period. Based on the low $\delta^{15}N$ and $\delta^{18}O$ values (1–2‰) measured during active NO_3^- export under high-flow conditions, this source signature is indicative of synthetic fertilizer and soybean biological N fixation (Kendall et al., 2007), in agreement with source attribution from the TREND-Nitrogen data set.

Despite the strong seasonality of NO_3^- concentrations and isotopes, significant in-season deviations were observed across the 3 years. Specifically, the period between the summer of 2021 and the winter of 2022 experienced an unusually wet condition (see mark above the upper axis of Figure 3), with total discharge ranked as the third highest for this period between 1994 and 2023. NO_3^- concentrations measured during this wet period were notably higher than those observed in the fall and winter of 2021 and 2023, which largely dampened the typical seasonality of NO_3^- concentrations for 2022 (Figure 3a). Additionally, the highest $\delta^{15}N$ and $\delta^{18}O$ values were also measured during this period (Figures 3b and 3c). In contrast, a dry spell occurred between the summer of 2022 and the winter of 2023 (Figure 3a), with total discharge ranked as the third lowest for this period over the 30 years. During this dry period, NO_3^- concentrations were very low (<0.5 mg N L^{-1}) to nondetectable, and highly scattered variations were observed for both $\delta^{15}N$ and $\delta^{18}O$ (Figure 4).

3.1.2. Seasonal NO_3^- Concentration-Isotopes-Discharge Relationships

The NO_3^- concentration-discharge relationship can be well characterized by the piecewise power law function for each of the three study years (Figure 5a). The estimated threshold discharge (±1 SE) was 0.42 ± 0.14, 0.36 ± 0.07, and 0.51 ± 0.18 mm d^{-1} for the three years, respectively, representing the 53rd, 41st, and 79th percentiles of discharge for each year. This range of threshold discharge is consistent with a previous study based on 33 watersheds of various sizes in this region (Marinos et al., 2020). Below these thresholds, NO_3^- export

19447973, 2025, 10, Downloaded from https://agupubs.onlinelibrary.wiley.com/doi/10.1029/2024WR039718 by Readcube (Labtiva Inc.), Wiley Online Library on [28/10/2025]. See the Terms and Conditions (https://onlinelibrary.wiley.com/terms-and-conditions) on Wiley Online Library for rules of use; OA articles are governed by the applicable Creative Commons License

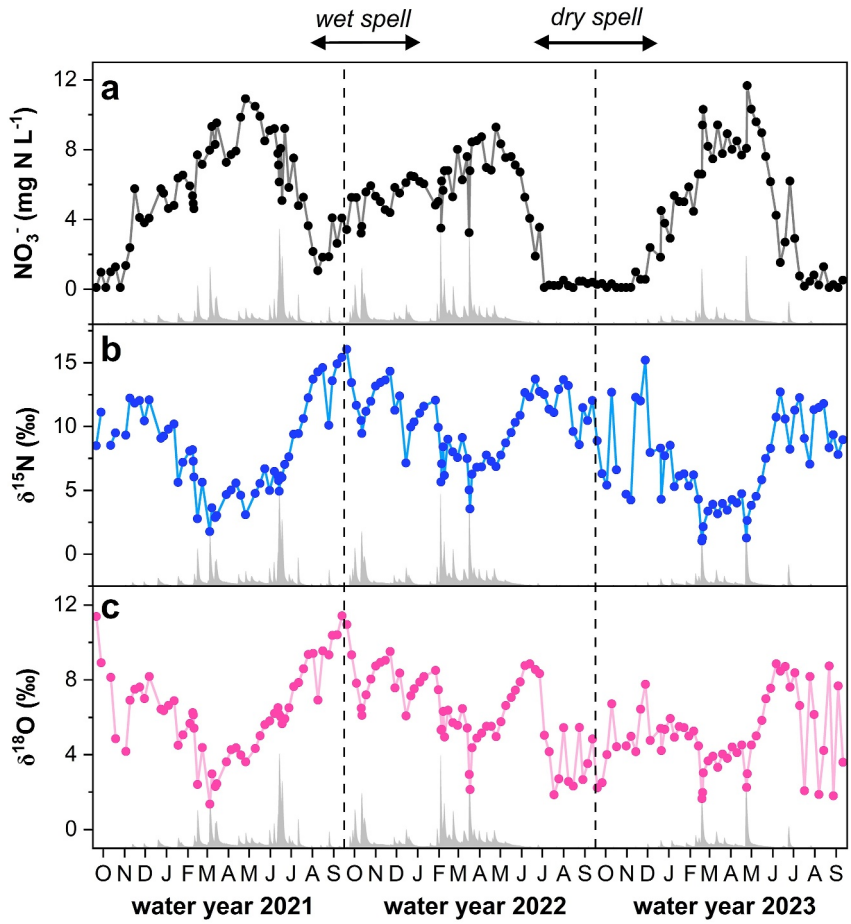

Figure 3. Temporal variations in NO_3^- concentration (a), $\delta^{15}N$ (b), and $\delta^{18}O$ (c) from 2021 to 2023. Daily discharge is also shown to aid interpretation. Vertical dashed lines mark the division between water years. Periods characterized by wet and dry spells are marked by double arrows above the upper axis.

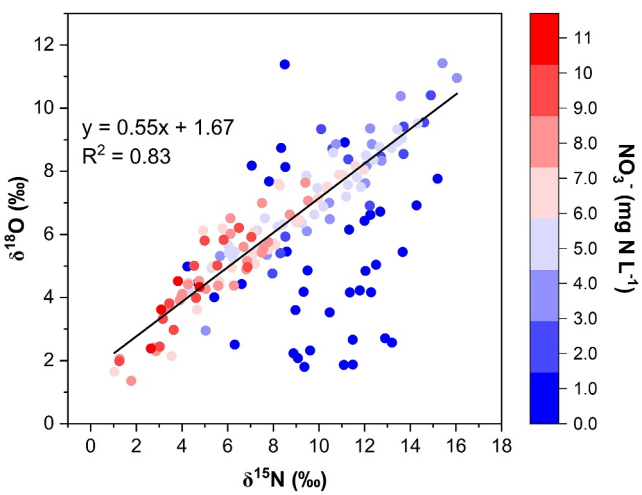

Figure 4. Biplot of $\delta^{15}N$ and $\delta^{18}O$ values with NO_3^- concentration displayed as a color contour. The linear fit is applied to $\delta^{15}N$ and $\delta^{18}O$ with corresponding NO_3^- concentrations ≥1 mg N L^{-1}.

exhibited flushing behaviors, with the power law exponents of 0.57 ± 0.06, 1.06 ± 0.08, and 0.85 ± 0.05 for the 3 years. When discharge exceeded these threshold values, the power law exponents decreased to 0.01 ± 0.08, −0.11 ± 0.08, and 0.05 ± 0.15 for the respective years, indicating a chemostatic export regime (Godsey et al., 2009).

Both $\delta^{15}N$ and $\delta^{18}O$ values displayed a breaking point behavior with discharge (Figures 5b and 5c). Specifically, NO_3^- isotope values were variable but tended to increase with discharge when discharge was below approximately 0.1 mm d^{-1}. Interestingly, while NO_3^- concentration variations were largely dampened under high-flow conditions (Figure 5a), both $\delta^{15}N$ and $\delta^{18}O$ values consistently declined as discharge increased beyond about 0.1 mm d^{-1} (Figures 5b and 5c). To avoid fitting piecewise relationships through scattered isotope values under low-flow conditions, we adopted the threshold discharge from the piecewise concentration-discharge relationships and fitted linear relationships to NO_3^- isotopes and log-discharge over the high-flow range where NO_3^- export was characterized by chemostasis. The negative linear relationships with discharge are significant for both $\delta^{15}N$ and $\delta^{18}O$ (ordinary linear regression, $P < 0.05$), except for $\delta^{18}O$ in 2021. The lack of a significant relationship in 2021 is mainly due to two large flow events during the summer of 2021 (see discharge around 1 July 2021, in

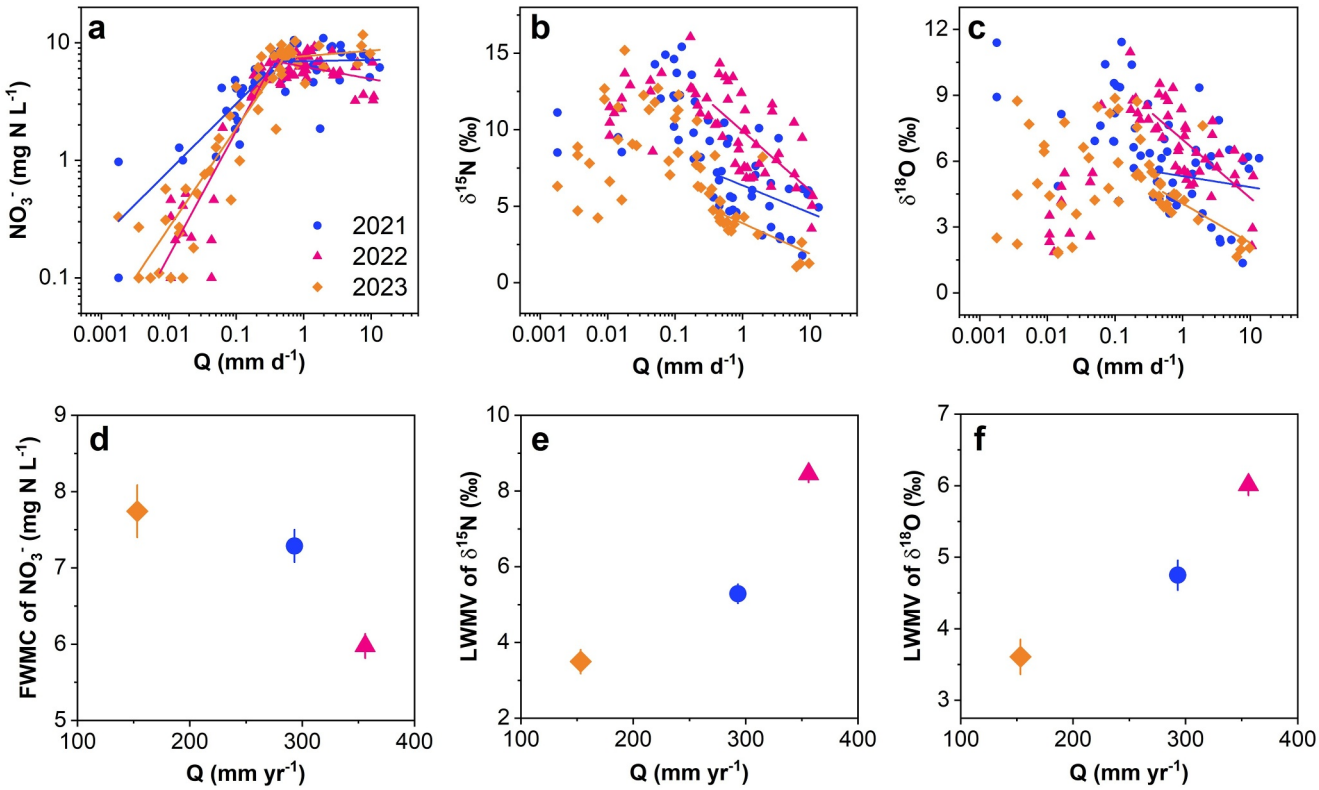

Figure 5. (a–c) Relationships between measured NO_3^- concentrations, NO_3^- isotopes, and discharge. The regression fits in panel (a) represent piecewise power law relationships between NO_3^- concentrations and discharge. The regression fits in panels (b, c) represent linear relationships between NO_3^- isotopes and log-discharge when discharge exceeded the thresholds identified in the concentration-discharge relationships. (d–f) Interannual variations in NO_3^- concentrations, NO_3^- isotopes, and discharge.

Figure 3), combined with relatively high $\delta^{18}O$ values observed during these events (Figure 3c), which introduced some hysteresis into the isotope-discharge relationship for that year.

3.1.3. Interannual NO_3^- Concentration-Isotopes-Discharge Relationships

At the interannual scale, the FWMC of NO_3^- varied only limitedly from 6.0 to 7.7 mg N L^{-1} across the 3 years, despite a twofold increase in annual discharge (Figure 5d). This aligns well with the concept of long-term chemostasis previously established for this region. However, the LWMV of $\delta^{15}N$ and $\delta^{18}O$ varied by 5.0 and 2.4‰, or 86% and 50% of their respective mean values across the three study years. Specifically, the lowest LWMV of $\delta^{15}N$ and $\delta^{18}O$ were observed in the drier 2023, while the highest occurred in the wetter 2022, leading to a positive relationship with annual discharge for both $\delta^{15}N$ and $\delta^{18}O$ (Figures 5e and 5f). These interannual variations in NO_3^- isotopes are consistent with the distinct isotope-discharge relationships observed at the seasonal scale (Figures 5b and 5c). Particularly, under similar high-flow conditions, NO_3^- isotopes were significantly lower in 2023, while significantly higher in 2022, as indicated by the vertical offsets between the fitted linear relationships (Figures 5b and 5c).

3.2. Water Age Results

The calibration results of the water age model are presented in Table 1, while the frequency distributions of behavioral parameter sets are shown in Figure S3 of Supporting Information S1. The SAS function parameters for Q_{HS} ($k_{QHS,wet}$ and $k_{QHS,dry}$) were robustly identified, with $k_{QHS,wet}$ being very close to the lower limit of the initial range (i.e., 0.1) and significantly lower than $k_{QHS,dry}$. This suggests that Q_{HS} has a strong preference for young water under wet conditions, but this affinity weakens and eventually shifts toward a slight old-water preference as the watershed becomes drier (i.e., $k_{QHS,dry}$: 1.11–3.16). Although the behavioral range of k_{QRP} spans a wide interval (i.e., 1.17–9.69), it consistently indicates that Q_{RP} preferentially samples older water from storage. As a

19447973, 2025, 10, Downloaded from https://agupubs.onlinelibrary.wiley.com/doi/10.1029/2024WR039718 by Readcube (Labtiva Inc.), Wiley Online Library on [28/10/2025]. See the Terms and Conditions (https://onlinelibrary.wiley.com/terms-and-conditions) on Wiley Online Library for rules of use; OA articles are governed by the applicable Creative Commons License

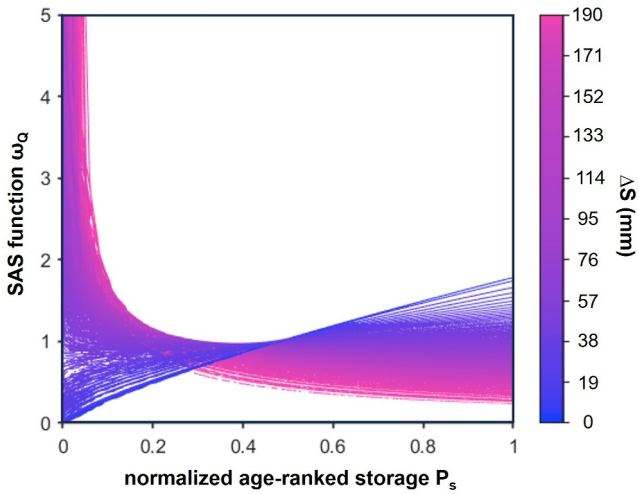

Figure 6. Variations in the composite SAS function for total discharge as a function of the storage anomaly ΔS. The composite SAS function is parameterized using the optimal transport parameter set derived from the water age model calibration.

result, the composite SAS function for total discharge (ω_Q) exhibits a strong inverse storage effect (Harman, 2015) in response to variations in ΔS, with a marked preference for young water under high-flow conditions (i.e., high ΔS) and a modest old water preference when the watershed is dry (i.e., low ΔS) (Figure 6).

The SAS function parameter for ET (u_{ET}) and initial storage (S_0) were not uniquely identified by model calibration. Based on the behavioral range of u_{ET} (0.42–0.99), ET appears to sample water uniformly from a pool spanning from the younger half of storage to the entire storage. Similarly, estimates of S_0 range from 500 to 2500 mm, although lower values close to 1000 mm are more likely to yield good model performance (Figure S3 in Supporting Information S1). This estimated range of S_0 is broader but comparable to storage estimates for tile drainage generation and Cl^- transport at the outlets of individual tile drains (811–1166 mm) (Yu et al., 2023). The low identifiability of SAS functions for ET and total water storage is a common issue in transit time studies and may be attributed to several factors, including the lack of constraints on tracer movement via ET, as well as uncertainties in the magnitudes and timescales of tracer input (Benettin et al., 2017; Hrachowitz et al., 2015; Rodriguez et al., 2018).

The simulated daily Cl^- concentrations in discharge for the entire 30-year period are shown in Figure S4a of Supporting Information S1, with results from 2021 to 2023 highlighted in Figure 7a. Despite uncertainties in some SAS model parameters, the model successfully reproduces the seasonal fluctuations in Cl^- concentration, as well as the large and often episodic declines during storm events. This is supported by high KGE_{Cl} values for the behavioral simulations over the 30-year period (0.72–0.74). At the interannual scale, simulated Cl^- FWMC agrees with observations well (Figure S5a in Supporting Information S1), with Pearson's r ranging from 0.59 to 0.73 across the behavioral simulations (Figure S5b in Supporting Information S1). Finally, the model accurately reproduces the strong dilution pattern in the Cl^--discharge relationship throughout the 30-year period (Figure 7b), indicating high fidelity in the water selection behaviors represented by the model.

We retrieved the median age of discharge from behavioral model simulations, which are shown in Figure S4b of Supporting Information S1 for the entire 30-year period and in Figure 7c for 2021 to 2023. The magnitude of median age varies significantly among different parameter sets, as indicated by the wide envelope of behavioral simulations (Figure S4b in Supporting Information S1 and Figure 7c). This variation is largely driven by the uncertainty in total storage, which controls the timescales of the transport processes. However, all parameter sets produced very similar median age dynamics, with pronounced decreases during storm events and substantial increases under drier conditions. Specifically, the median water age remained low during the wet spell between the summer of 2021 and the winter of 2022, reflecting intensified hydrologic transport, while the dry spell between the summer of 2022 and the winter of 2023 was characterized by a broad plateau in the modeled median water age (Figure 7c). Using the behavioral parameter sets, we estimated the flow-weighted marginal age distribution for the entire 30-year period (Figure 7d). The mean median age of discharge varied between 51 and 399 days among all behavioral simulations, with the optimal simulation yielding a mean median age of 119 days. For 2021–2023, the wetter conditions in 2022 produced a lower mean median water age (82–407 days) compared to the drier 2023 (107–516 days).

3.3. NO_3^- Transport Modeling Results

Out of the 1,000 combined Pareto solutions, 44 were identified as behavioral parameter sets for the dynamic NO_3^- transport model. The resulting parameter ranges are present in Table 2, with the corresponding frequency distributions shown in Figure S7 in Supporting Information S1. These behavioral model realizations were based on four out of the 11 transport parameter sets used to drive the biogeochemical simulations. However, these four transport parameter sets represent a wide range of flow-weighted mean median age, from 70 to 399 days over the 30-year period. On the other hand, although many parameter sets met the KGE_{NO3} and $KGE_{\delta 18O}$ criteria for the

19447973, 2025, 10, Downloaded from https://agupubs.onlinelibrary.wiley.com/doi/10.1029/2024WR039718 by Readcube (Labtiva Inc.), Wiley Online Library on [28/10/2025]. See the Terms and Conditions (https://onlinelibrary.wiley.com/terms-and-conditions) on Wiley Online Library for rules of use; OA articles are governed by the applicable Creative Commons License

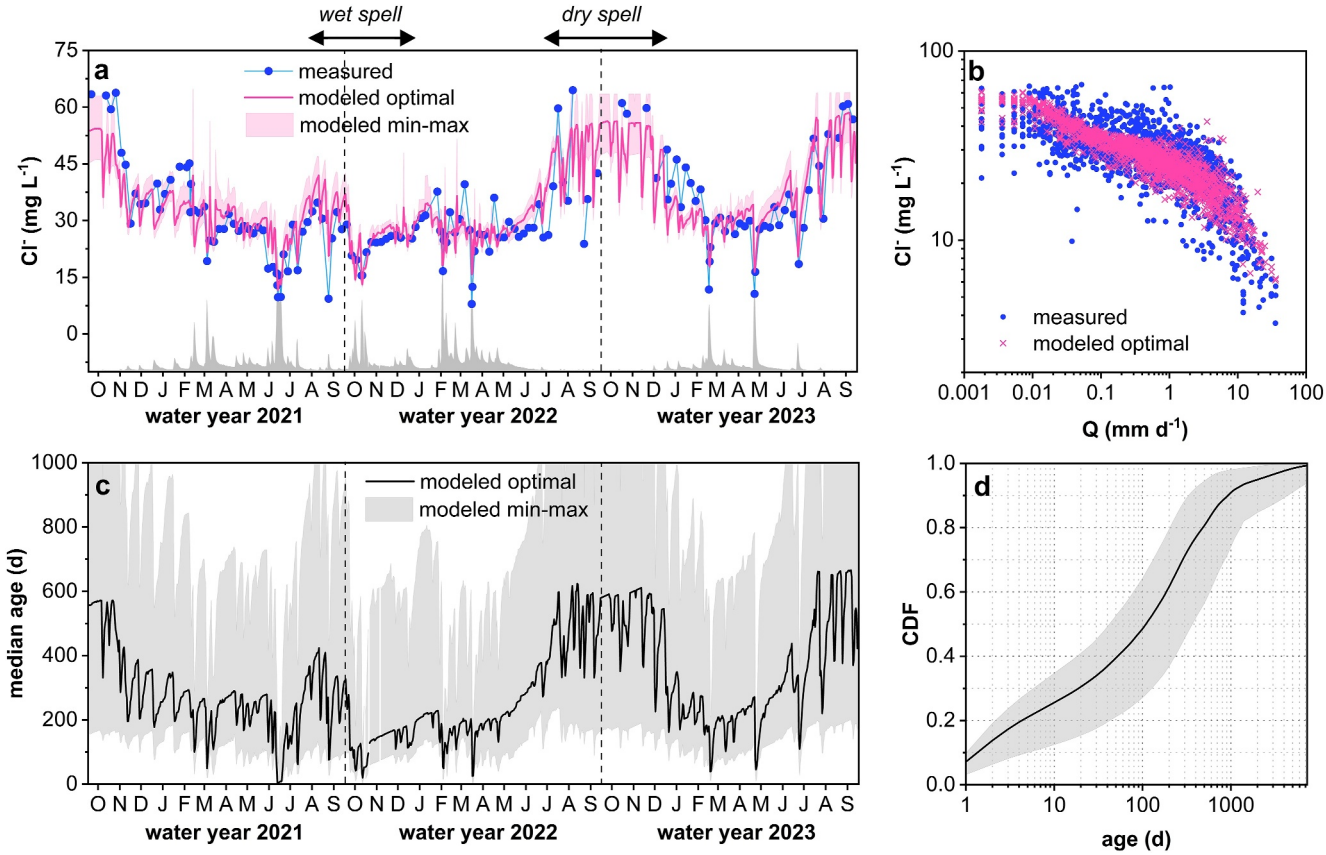

Figure 7. (a) Simulated daily Cl concentrations in discharge compared to measured data for 2021 to 2023. Daily discharge is also shown to aid interpretation. (b) Comparison between modeled and measured Cl^--discharge relationship over the 30-year period using the optimal parameter set. (c) Median age of discharge for 2021 to 2023. (d) Flow-weighted marginal age distribution for the 30-year study period. Water ages greater than 7,300 days (i.e., 20 years) are grouped into the 7,300-day category. In panels (a, c, d), solid lines represent simulations based on the optimal parameter set, while shaded bands indicate the envelope of behavioral simulations. For clarity, the upper bound of the envelope, which extends to approximately 10,000 days, is not shown. Vertical dashed lines in panels (a, c) mark the division between water years.

static model, none satisfied the prior constraint needed to reproduce the correct rank order of the LWMV of $\delta^{18}O$. Specifically, the static model consistently predicted the lowest LWMV of $\delta^{18}O$ for 2022 (Figure S8 in Supporting Information S1), whereas, in reality, it was the highest among the three years. This mismatch stems from the static model's inability to account for wetness-related feedbacks: the wetter conditions in 2022 led to a higher proportion of younger, which, in the absence of wetness-dependent denitrification, resulted in less denitrified NO_3^- and lower modeled $\delta^{18}O$ values in the stream. More details of the calibration results for the static model are provided in Text S4 of Supporting Information S1. Based on these findings, we concluded that the wetness dependence of denitrification, as incorporated into the dynamic model, is justified, and we therefore focused on the results from the dynamic model for subsequent analysis.

The behavioral C_{lim} values showed significant variations across the four seasons, with the highest C_{lim} value estimated for spring, followed by winter (Table 2; Figure S7 in Supporting Information S1). In contrast, summer and fall generally had low C_{lim} values (i.e., <10 mg N L^{-1}). The estimated r_d ranged from 0.070 to 0.69 $days^{-1}$ and was significantly higher than the estimated r_n (i.e., 0.0012–0.0040 $days^{-1}$). Therefore, NO_3^- concentration of a newly arriving water parcel quickly approaches C_{lim} within a timescale of a few days to two weeks, while the timescale of denitrification extends to at least several hundred days (Figure S14 in Supporting Information S1). Additionally, the estimated $^{18}\alpha$ (i.e., 1.010–1.038) corresponds to a denitrification isotope effect of 10–38‰, which falls within the range previously reported for denitrifying pure cultures and soil incubations (Denk et al., 2017; Granger et al., 2008), while the estimated $\delta^{18}O_{nit}$ (−0.8–0.8‰) is at the upper end of the range based on the current understanding of nitrification isotope effects (i.e., −15 to 2‰) (Boshers et al., 2019). Finally, the

19447973, 2025, 10, Downloaded from https://agupubs.onlinelibrary.wiley.com/doi/10.1029/2024WR039718 by Readcube (Labtiva Inc.), Wiley Online Library on [28/10/2025]. See the Terms and Conditions (https://onlinelibrary.wiley.com/terms-and-conditions) on Wiley Online Library for rules of use; OA articles are governed by the applicable Creative Commons License

19447973, 2025, 10, Downloaded from https://agupubs.onlinelibrary.wiley.com/doi/10.1029/2024WR039718 by Readcube (Labtiva Inc.), Wiley Online Library on [28/10/2025]. See the Terms and Conditions (https://onlinelibrary.wiley.com/terms-and-conditions) on Wiley Online Library for rules of use; OA articles are governed by the applicable Creative Commons License

estimated S_m (i.e., 106–138 mm) was well-constrained by model calibration, indicating that denitrification activity begins to be limited when storage is about 70–100 mm lower than the wettest condition observed over the 30-year period.

The simulated NO_3^- concentrations and $\delta^{18}O$ values are shown in Figure 8 for comparison with measured data. In general, the model well reproduced the seasonal variability of measured NO_3^- concentrations and $\delta^{18}O$ in discharge (Figures 8a and 8e). Moreover, the model successfully reproduces the piecewise variations in NO_3^- concentrations and $\delta^{18}O$ with discharge, particularly for their spread and variability under high-flow conditions (Figures 8b and 8h). Although the FMWC of NO_3^- was not used as a constraint during model calibration, it was accurately simulated across the 3 years (Figure 8d). However, it is also noticeable that the model did not simulate NO_3^- concentrations and isotopes well during certain periods. For example, NO_3^- concentrations were significantly underestimated during the wet fall and winter of 2022 (see October 2021 to February 2022 in Figure 8c), while the corresponding $\delta^{18}O$ values were significantly overestimated (Figure 8g). Following this wet period and into the spring of 2022, the residual patterns shifted, with the model generally overestimating the NO_3^- concentrations and significantly underestimating the $\delta^{18}O$ values. While the compensating model residuals for NO_3^- concentrations resulted in a well-simulated FWMC of NO_3^- for 2022 (Figure 8d), the large underestimation of $\delta^{18}O$ values during the spring of 2022 carried over to the annual scale, leading to a significant underestimation of the LWMV of $\delta^{18}O$ by 1‰ (Figure 8h).

Based on all behavioral simulations, the wetness scalar of denitrification, θ_a, varied between 0.17 and 1 over the three study years (Figure 9a). While high θ_a values were consistently estimated for high-flow conditions each spring, θ_a remained high between late 2021 and early 2022 due to the unusual wet condition during this period. In contrast, the dry spell from late 2022 to early 2023 was characterized by significantly reduced θ_a values, indicating largely reduced denitrification rates. Moreover, the effect of this dry spell seems to carry into the following spring, resulting in lower θ_a values during that period compared to the springs of the previous 2 years. This variability in θ_a closely mirrors that of median water age (i.e., compare Figures 7c and 9a), with discharge dominated by young water showing higher θ_a values, and vice versa. At the annual scale, the flow-weighted mean θ_a, based on all behavioral simulations, was significantly higher in the wetter 2022 and significantly lower in the drier 2023 ($P < 0.05$; Figure 9b).

Due to the direct control of θ_a on actual denitrification rates, the temporal variability of RT_{50} closely followed that of θ_a (Figure 9c). However, high uncertainties were found in the estimated RT_{50} values due to uncertainties from both transport and biogeochemical parameter sets. In general, the flow-weighted mean annual RT_{50} values ranged from 200 to 800 days across different behavioral model simulations, with significantly lower values in 2022 and significantly higher values in 2023 ($P < 0.05$; Figure 9d). Finally, the estimated Da_{50} was highly sensitive to changes in hydrologic regimes, with lower values indicating intensified NO_3^- transport during peak-flow conditions (Figure 9e). At the annual scale, the flow-weighted mean Da_{50} generally ranged between 0.2 and 2 (Figure 9f). Interestingly, while RT_{50} was significantly lower for the wetter 2022 compared to the drier 2023, the estimated Da_{50} did not differ significantly between these two years based on all behavioral runs (Figure 9f). This lack of difference in Da_{50} is due to the significantly lower mean median water age for 2022 compared to 2023, which offsets the effects of changing wetness conditions on the denitrification timescale.

4. Discussion

4.1. How Do Water Age, NO_3^- Concentration, and NO_3^- Isotopes Vary With Discharge, and What Can That Tell Us About the Coupling of Watershed Hydrologic and Biogeochemical Functions?

4.1.1. Riparian Controls and NO_3^- Flushing During Low-Flow Periods

Water age, NO_3^- concentration, and NO_3^- isotopes each exhibited distinct variations with discharge (Figures 5–7). By differentiating between riparian and hillslope flows using the composite SAS approach, the water age modeling revealed an inverse storage effect, whereby larger storage promotes the release of younger water. Conversely, an older water preference was identified for the riparian flow (i.e., $k_{QRP} > 1$). This old water preference suggests that, under the driest conditions, discharge is primarily sustained by advective transport via deep and long groundwater flow paths that remain connected to the stream network. During these periods, the stream network is highly contracted, and flow generation is likely concentrated in riparian areas or other near-stream

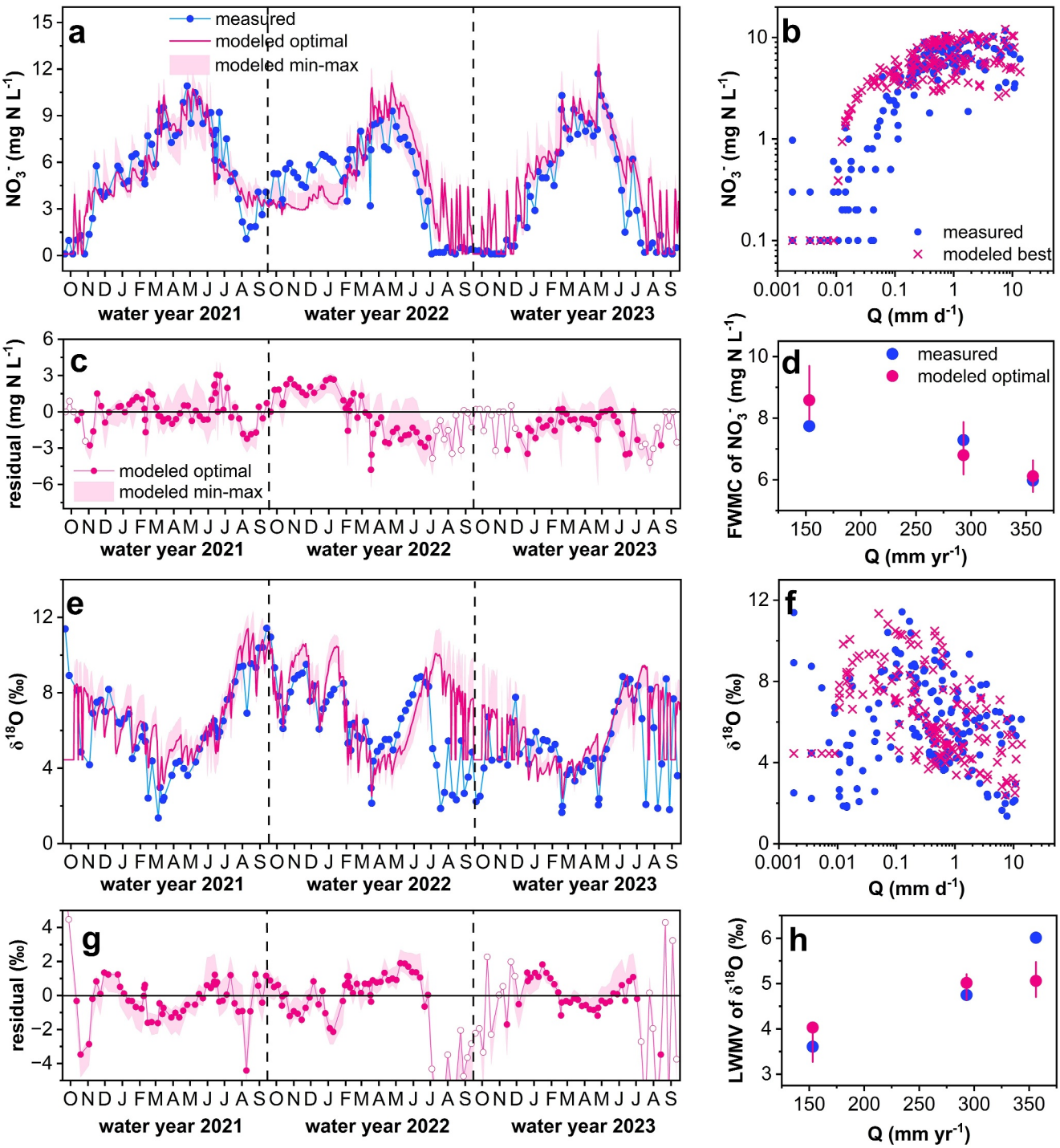

Figure 8. Comparison of measured and modeled NO_3^- concentrations and $\delta^{18}O$ values using the dynamic model as functions of time (a, e) and discharge (b, f). Solid lines in panels (a, e) represent simulations based on the optimal parameter set, while shaded bands indicate the envelope of behavioral simulations. Model residuals for NO_3^- concentrations and $\delta^{18}O$ values are shown as a function of time in panels (c, g). Open symbols represent sampling dates with NO_3^- concentration lower than 1 mg N L^{-1}, which were not included in the model calibration. Vertical dashed lines in panels (a, c, e, g) mark the division between water years. Modeled FMWC of NO_3^- and LWMV of $\delta^{18}O$ are compared to measured values in panels (d, h). Solid symbols denote simulations based on the optimal parameter set. Error bars denote the min-max range based on all behavioral simulations.

environments (e.g., hyporheic zones) along the downstream main stem (Kaandorp et al., 2021; Knapp et al., 2022; van Meerveld et al., 2019). In contrast, flow contributions from tile-and-ditch systems in the headwater regions largely cease due to enhanced crop ET (Yu et al., 2023).

19447973, 2025, 10, Downloaded from https://agupubs.onlinelibrary.wiley.com/doi/10.1029/2024WR039718 by Readcube (Labtiva Inc.), Wiley Online Library on [28/10/2025]. See the Terms and Conditions (https://onlinelibrary.wiley.com/terms-and-conditions) on Wiley Online Library for rules of use; OA articles are governed by the applicable Creative Commons License

10.1029/2024WR039718

19447973, 2025, 10, Downloaded from https://agupubs.onlinelibrary.wiley.com/doi/10.1029/2024WR039718 by Readcube (Labtiva Inc.), Wiley Online Library on [28/10/2025]. See the Terms and Conditions (https://onlinelibrary.wiley.com/terms-and-conditions) on Wiley Online Library for rules of use; OA articles are governed by the applicable Creative Commons License

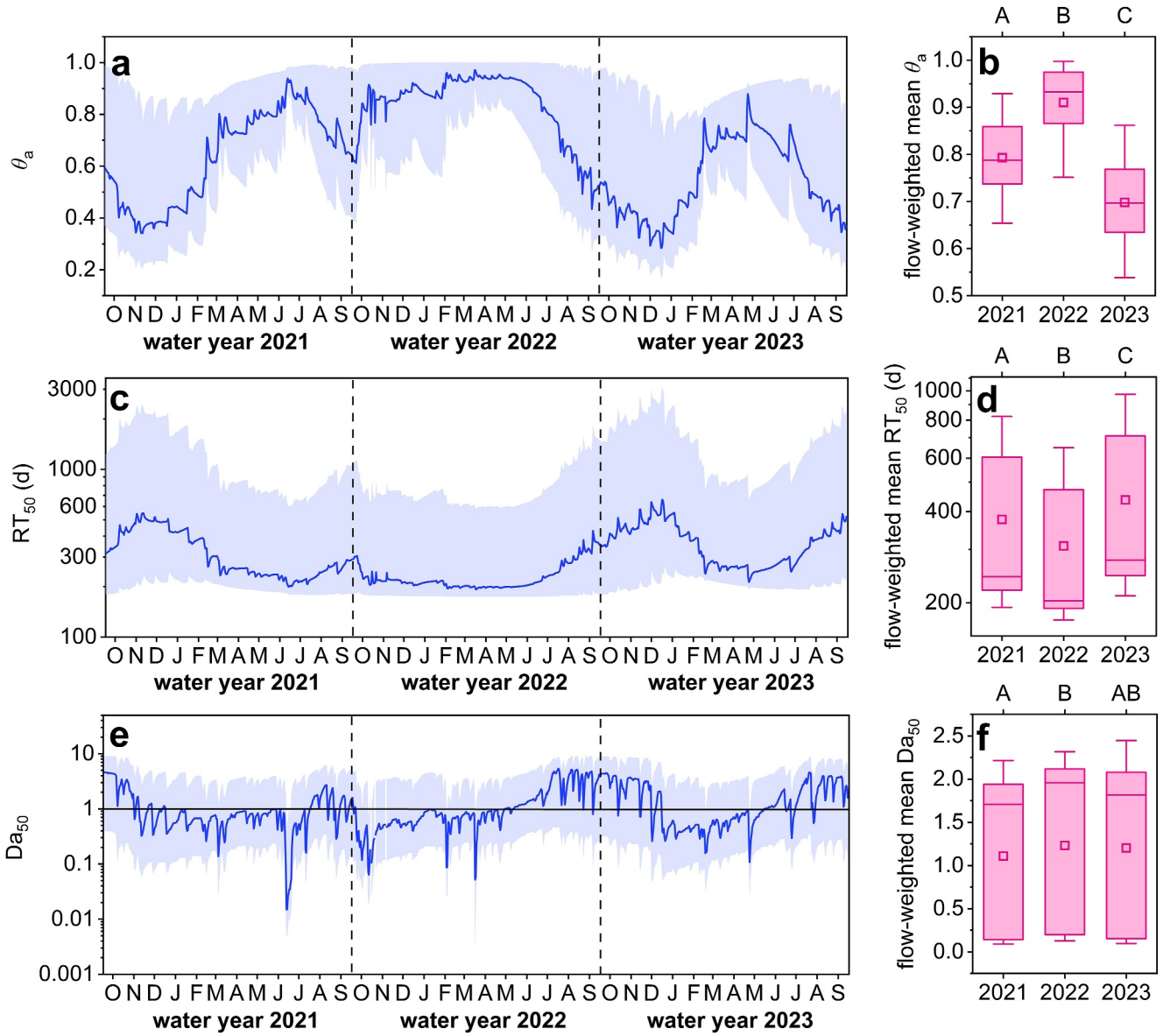

Figure 9. Temporal variations in estimated θ_a (a), RT_{50} (c), and Da_{50} (e) during 2021–2023. Solid lines represent simulations based on the optimal parameter set, while shaded bands indicate the envelope of behavioral simulations. Note that Da_{50} is displayed on a logarithmic scale. Flow-weighted mean annual θ_a, RT_{50}, and Da_{50} are shown as boxplots in panels (b, d, f) for the three study years. The boxes show the 25–75th percentiles of estimates based on all behavioral simulations for each year, with the median value shown with a horizontal line inside each box and the mean value as a square. Error bars show minimum and maximum values based on all behavioral simulations. Letters above the boxes indicate significant differences between different years.

During these dry periods, NO_3^- concentrations in discharge were very low or non-detectable (Figure 3a). If this depletion were primarily caused by denitrification along extended flow paths, we would expect strong and coupled enrichments in $\delta^{15}N$ and $\delta^{18}O$ values. However, measured NO_3^- isotopes were highly variable but generally low during these periods, especially for $\delta^{18}O$ (Figures 3b, 3c, and 4). These seemingly paradoxical results may be explained by heterogeneity in both N cycling and flow path connectivity within downstream riparian areas. Riparian zones are known to act as hot spots for N removal and retention. In the absence of direct fertilization, these areas are likely N-limited, which could promote the uptake of NO_3^- from groundwater by riparian plant and microbial communities. Recycling of this assimilated N, together with mixing of NO_3^- produced from mineralization and nitrification of indigenous riparian soil N, would erase original groundwater denitrification signals, resulting in low $\delta^{18}O$ values. In addition, recent studies have highlighted the complexity of flow regimes in riparian areas, shaped by preferential flow pathways via macropores and soil pipes (Hester &

10.1029/2024WR039718

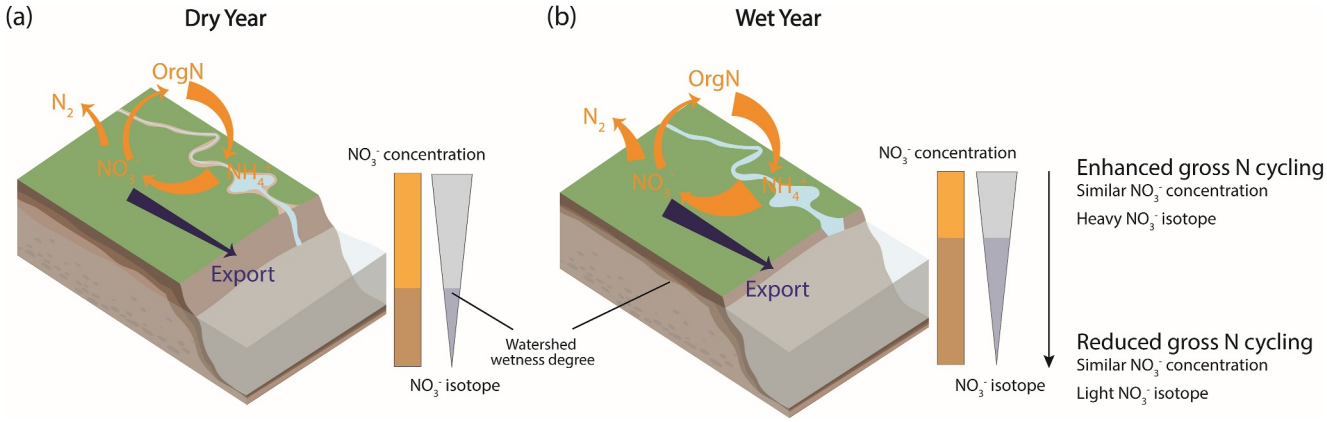

Figure 10. Conceptual diagram illustrating concentration-isotope-age-discharge relationships at the interannual scale. The intensity of gross N cycling through mineralization, nitrification, and denitrification is regulated by antecedent moisture conditions, with less intense cycling in drier years (a) and more intense cycling in wetter years (b). The effect of this wetness-dependent N cycling is offset by storage-dependent flow path activation, which controls NO_3^- source mobilization and subsequent export, leading to NO_3^- chemostasis at the interannual scale. While NO_3^- concentration is co-regulated by N cycling and hydrologic transport, the interannual variability in gross N cycling is reflected in the NO_3^- isotopic signatures. In panels (a, b), the thickness of the arrows represents the gross rates of N cycling and export processes.

Fox, 2020; Moore et al., 2023; Redder et al., 2021). When oriented horizontally toward the stream, these pathways can enhance lateral connectivity and allow bypassing of riparian N retention zones, even during overall stream network contraction (Hester & Fox, 2020). Thus, the high variability of NO_3^- isotopes observed during these low-flow periods likely reflects a mixed signal of groundwater denitrification and recycled N from riparian areas, modulated by shifting riparian flow regimes in response to summer/fall precipitation events. We note that these localized dynamics are not represented in the water age or NO_3^- transport models, which were parsimoniously designed to simulate dominant hydrologic and biogeochemical processes during active NO_3^- export (i.e., under high-flow conditions). Future work should focus on characterizing representative riparian zones to better understand their flow regimes and N cycling capacities, particularly under low-flow conditions, to improve model process representation.

As wetness increases, such as after several precipitation events in early winter, groundwater may rise and intersect more of the high-porosity, high-conductivity glacial till in the shallow subsurface. Consequently, the rising groundwater table may activate shallower and shorter flow paths, leading to higher flows and an increased contribution of young water to discharge (Kim & Harman, 2022). Since the subsurface NO_3^- gradient typically increases toward the surface due to both surface N inputs and groundwater denitrification, the flushing behavior of NO_3^- observed during this transition period can be well explained by the progressive activation of shallower flow paths and near-surface NO_3^- source zones as the groundwater table rises (Seibert et al., 2009). These coupled variations between discharge, water age, and NO_3^- concentration align with the inverse storage effect estimated for hillslope flow and the inverse relationship between water age and NO_3^- concentration captured in the NO_3^- transport model.

However, measured NO_3^- isotopes during this flushing phase of NO_3^- export exhibit more complexity. Specifically, both $\delta^{15}N$ and $\delta^{18}O$ values increased with discharge when discharge was lower than approximately 0.1 mm d^{-1}, but eventually decreased once discharge exceeded 0.1 mm d^{-1} but remained below the threshold discharge for chemostatic export (Figures 5b and 5c). This piecewise pattern suggests that lateral connectivity between the groundwater system and the stream was initially patchy due to dry antecedent conditions (Zimmer & McGlynn, 2018). During this early wetting-up phase, the variability of NO_3^- isotope values remained high, and the general increase in $\delta^{15}N$ and $\delta^{18}O$ values with discharge likely reflects mixing between isotopically enriched groundwater NO_3^- and isotopically lighter, riparian-recycled NO_3^-. As the groundwater system becomes fully connected, contributions from shallow, less denitrified flow paths dominate, resulting in declining NO_3^- isotope values with increasing discharge.

19447973, 2025, 10, Downloaded from https://agupubs.onlinelibrary.wiley.com/doi/10.1029/2024WR039718 by Readcube (Labtiva Inc.), Wiley Online Library on [28/10/2025]. See the Terms and Conditions (https://onlinelibrary.wiley.com/terms-and-conditions) on Wiley Online Library for rules of use; OA articles are governed by the applicable Creative Commons License

19447973, 2025, 10, Downloaded from https://agupubs.onlinelibrary.wiley.com/doi/10.1029/2024WR039718 by Readcube (Labtiva Inc.), Wiley Online Library on [28/10/2025]. See the Terms and Conditions (https://onlinelibrary.wiley.com/terms-and-conditions) on Wiley Online Library for rules of use; OA articles are governed by the applicable Creative Commons License

4.1.2. NO_3^- Chemostasis Under Seasonal High-Flow Conditions

As wetness further increases during winter and spring, the groundwater table may rise to the depth of the tile drains, activating the tile drainage systems. This activation significantly enhances the contribution of young water to discharge due to the dramatically increased connectivity between surface soils and the stream (Yu et al., 2023). At the watershed scale, this increase in young water contribution is further amplified by the substantial increase in drainage density as facilitated by the dense network of outlet ditches (van Meerveld et al., 2019). Despite the dampened variability in NO_3^- concentrations (i.e., chemostasis), both $\delta^{15}N$ and $\delta^{18}O$ values consistently declined with discharge during these wettest periods (Figures 5b and 5c), indicating a growing dominance of nitrification over denitrification. These strong inverse relationships of water age and NO_3^- isotopes with discharge, observed in parallel with chemostatic NO_3^- export, are remarkably consistent with our previous findings at the scale of individual tile drain outlets in this area (Hu et al., 2024; Yu et al., 2023). This consistency across spatial scales highlights the functional homogeneity of intensively tile-drained agricultural watersheds like the UER (Basu, Rao, et al., 2010), which facilitates the rapid transmission of tile drainage signals to the watershed scale.

In line with our interpretation at the tile-drain scale, the NO_3^- chemostasis observed under high-flow conditions can be explained by an increasing contribution of surface soil water via vertical preferential flow paths (Yu et al., 2023). It is well established that an extensive network of macropores, associated with root channels, earthworm burrows, desiccation cracks, can develop in fine-textured and densely rooted agricultural soils (Vidon & Cuadra, 2010; Williams et al., 2016). When antecedent soil moisture is high, these vertical preferential flow paths can be activated in surface soil layers during and immediately following large storm events (Cain et al., 2022), causing bypassing of the lower soil matrix due to reduced matrix-macropore interactions (Hrachowitz et al., 2013; Klaus et al., 2013). Preferential recharge at an already high groundwater table may activate short horizontal flow paths toward the tile drain, contributing a large amount of young water and isotopically light NO_3^- to the stream.

Importantly, since these preferential flows often consist mainly of event water and surface soil water from recent precipitation, the NO_3^- concentration in these flows may be lower than that of soil matrix flows due to dilution and/or limited NO_3^- mass transfer. This is supported by results from the NO_3^- transport model, which indicate that the timescale of NO_3^- mass transfer is about 2–14 days (Table 2). Consequently, water originating from surface soil that is significantly younger than 2 weeks may have similar NO_3^- concentrations as deeper soil water that has undergone some denitrification (Figure S14 in Supporting Information S1). Thus, the dilution and/or limited NO_3^- mass transfer facilitated by the activation of vertical soil preferential flows can explain the apparent NO_3^- chemostasis observed under high-flow conditions. However, since NO_3^- isotopes are specific to biogeochemical processing and not affected by dilution, the increasing contribution of surface-derived NO_3^- via preferential flow is clearly manifested in the NO_3^- isotope-discharge relationship.

In summary, the distinct relationships between NO_3^- concentrations, isotopes, water age, and discharge observed in the UER are largely driven by the dynamic responses of groundwater depth to changing wetness conditions and by soil matrix-macropore interactions that control the activation of vertical preferential flow paths. Although our discussion focuses on flow path variations as wetness increases, the absence of strong hysteretic behavior in the observed concentration-isotope-discharge relationships suggests that these insights are also applicable to drying conditions at the seasonal scale. We conclude that combining NO_3^- concentration-isotopes-discharge relationships with time-variant water transit times provides a more nuanced understanding of NO_3^- export regimes. The strength of this integrated approach stems from the complementary abilities of SAS functions and NO_3^- isotopes to resolve co-occurring flow path variations and N transformation processes, which cannot be achieved through C-Q analysis alone.

4.2. How Do the Biogeochemical Processes Driving NO_3^- Export Respond to Changes in Antecedent Wetness Conditions, and Can We Discern This Response at the Watershed Scale?

4.2.1. NO_3^- Source Availability and Wetness-Dependent Denitrification

Both NO_3^- concentrations and isotopes are well simulated by the dynamic NO_3^- transport model (Table 2; Figure 8). A key finding from the modeling results is that C_{lim} varied significantly across seasons, with higher values in spring and winter (Table 2). This seasonal pattern of C_{lim} mirrors the pattern observed in NO_3^- concentrations in discharge (Figure 3a), suggesting a strong connection between NO_3^- export and soil NO_3^-

19447973, 2025, 10, Downloaded from https://agupubs.onlinelibrary.wiley.com/doi/10.1029/2024WR039718 by Readcube (Labtiva Inc.), Wiley Online Library on [28/10/2025]. See the Terms and Conditions (https://onlinelibrary.wiley.com/terms-and-conditions) on Wiley Online Library for rules of use; OA articles are governed by the applicable Creative Commons License

dynamics. This is perhaps not surprising, given the high soil-stream connectivity in this intensively tile-drained watershed. Moreover, the seasonal variation in C_{lim} is supported by extensive observational evidence showing great variability in soil NO_3^- for typical corn-soybean production systems in this region. In the UER, N fertilizer applications typically occur in spring before corn planting or in late fall after the previous crop is harvested (Gentry et al., 2014). Rapid nitrification following the application of ammoniacal fertilizers, coupled with enhanced soil N mineralization under high soil moisture conditions, can explain the high C_{lim} values in spring and winter (Fernández et al., 2017). Conversely, during the growing season, soil NO_3^- concentrations can decline significantly due to crop uptake (Preza-Fontes et al., 2020). Although it is challenging to validate watershed-scale modeling results with localized measurements, the estimated magnitude and variability of seasonal C_{lim} values are consistent with NO_3^- concentrations measured in soil root zone leachates in this region (e.g., <1–60 mg N L^{-1}) (Maharjan et al., 2014). Therefore, this revealed seasonal variability in C_{lim} suggests that the NO_3^- chemostasis observed under seasonal high-flow conditions is a result of the synchronized dynamics of flow path activation, soil N cycling, and cropping practices, which converge to cause rapid NO_3^- mobilization during the winter-spring season.

The maximum denitrification rate constant r_n was estimated to range from 0.0012 to 0.0040 $days^{-1}$. The actual denitrification rate was lower due to variable antecedent conditions, as indicated by varying θ_a values (Figure 9a). Accounting for this wetness-dependence and based on all behavioral simulations, the flow-weighted mean actual denitrification rate for the entire 3-year period ranged between 0.0010 and 0.0037 $days^{-1}$. This range is in excellent agreement with the denitrification rate of 0.0025 $days^{-1}$ estimated by van der Velde et al. (2010) using a similar transit time-based method for a small tile-drained agricultural watershed in the Netherland. It is also consistent with denitrification rates reported in recent studies that applied SAS functions to constrain denitrification in agriculturally impacted watersheds (i.e., 0.0001 to 0.005 $days^{-1}$) (Borriero et al., 2024; Nguyen et al., 2022). Furthermore, Green et al. (2008) compiled measured denitrification rates based on naturally occurring gradients in excess N_2 for multiple shallow aquifers in U.S. agricultural areas. These rates varied between 1 and 23 μg N L^{-1} d^{-1} (Green et al., 2008). Assuming a mean C_{lim} value of 12.1 mg N L^{-1}, calculated by averaging the seasonal C_{lim} values based on the optimal model realization (Table 2), the initial zero-order rate of denitrification in the UER is estimated to range from 11 to 44 μg N L^{-1} d^{-1}, which is generally consistent with the range obtained from direct measurements. This comparison provides a certain degree of confidence in our estimated watershed-scale denitrification rates, which are notoriously difficult to quantify at field scales.

Importantly, the estimation of denitrification and its dependence on wetness conditions critically relies on the prior constraint imposed on the simulated LWMV of $\delta^{18}O$, which is, in turn, based on the simplifying assumption of a constant $\delta^{18}O_{nit}$ for the isotope simulation. Given the intrinsic linkage between $\delta^{18}O_{nit}$ and the $\delta^{18}O$ of source water (Boshers et al., 2019; Hu et al., 2024), if soil water $\delta^{18}O$ varied significantly over the three study years, it could compromise the validity of $\delta^{18}O$ as a calibration constraint. Similarly, since nitrification likely occurs in surface soil where O_2 is abundant, evaporative enrichment of $\delta^{18}O$-H_2O can influence the value of $\delta^{18}O_{nit}$.

However, we argue that neglecting the variability in $\delta^{18}O_{nit}$ should have a minor impact on the model results here, as the observed $\delta^{18}O$ dynamics in discharge was predominantly controlled by denitrification along subsurface transport. This control is reflected in the strong coupling between $\delta^{15}N$ and $\delta^{18}O$ values at event to interannual scales (Figure 4, Figures 5e, 5f), which cannot be explained by isotope effects acting solely on $\delta^{18}O$. Furthermore, across a wide range of discharge (i.e., from 0.1 mm d^{-1} to 10 mm d^{-1})—and, correspondingly, a broad span of water ages (Figure 7)—observed $\delta^{18}O$ values were consistently lower in the drier 2023, as indicated by the offsets in the $\delta^{18}O$-discharge relationship among the 3 years (Figures 5b and 5c). This trend cannot be explained by $\delta^{18}O_{nit}$ variability in NO_3^- source zones alone, which would affect NO_3^- isotopes in younger water but have no impact on the $\delta^{18}O$ values of NO_3^- in water older than the characteristic timescale of mobile-immobile mass transfer (i.e., up to 2 weeks as indicated by the behavioral values of r_d; Table 2). Altogether, these results reinforce that denitrification occurring along subsurface transport responds to changes in watershed wetness status. Future benchmarking studies that explicitly account for the variability of $\delta^{18}O_{nit}$ driven by water mixing, seasonal precipitation input, and evaporative enrichment are warranted to assess the relative controls of nitrification and denitrification on $\delta^{18}O$ dynamics at the watershed scale.

19447973, 2025, 10, Downloaded from https://agupubs.onlinelibrary.wiley.com/doi/10.1029/2024WR039718 by Readcube (Labtiva Inc.), Wiley Online Library on [28/10/2025]. See the Terms and Conditions (https://onlinelibrary.wiley.com/terms-and-conditions) on Wiley Online Library for rules of use; OA articles are governed by the applicable Creative Commons License

4.2.2. Mechanisms Driving Long-Term NO_3^- Chemostasis

Linking the identified wetness dependence of denitrification with the inverse storage effect in water selection behaviors provides further insights into the mechanisms driving long-term NO_3^- chemostasis. Specifically, in wetter years, high antecedent wetness conditions can enhance NO_3^- loss both through increased denitrification and greater NO_3^- mobilization due to more frequent activation of shallow flow paths. However, the observation that NO_3^- FWMC remained similar in the wetter 2022 compared to the drier 2023 suggests that wetter conditions may have also stimulated NO_3^- production via mineralization and nitrification, thereby accelerating gross NO_3^- cycling in the soil (Figure 10). Conversely, in the drier 2023, limited denitrification and suppressed soil NO_3^- production under dry antecedent conditions likely reduced the intensity of gross NO_3^- cycling (Figure 10). The impact of this reduced cycling on NO_3^- export may have been offset by simultaneously reduced NO_3^- mobilization, resulting in similar NO_3^- concentrations in leaching flows across wet and dry years.

Importantly, these coupled biogeochemical and hydrologic responses indicate a strong buffering capacity of NO_3^- production and mobilization within the soil source zone. Indeed, although C_{lim} varies seasonally, the ability of a constant set of C_{lim} values to reproduce observed NO_3^- concentrations and isotopes in both the wetter 2022 and the drier 2023 highlights, in an implicit way, a transport-limited system, where the amount of NO_3^- produced and mobilized is proportional to water fluxes through the source zone. This buffering capacity likely stems from the large soil N stocks characteristic of fertile Mollisols prevalent in the study region, which can sustain NO_3^- via mineralization and nitrification in response to variations in soil moisture. On the other hand, given this NO_3^- source buffering, if denitrification were constant and unresponsive to wetness conditions, NO_3^- FWMC would be higher in wetter years due to increased contributions from younger water, which tends to have NO_3^- concentrations closer to C_{lim}. Thus, interannual chemostatic behavior emerges from the coupled and proportional responses of soil NO_3^- production, denitrification, flow path activation to changing wetness conditions. The offsetting nature of these coupled responses leads to similar Da_{50} values across wet and dry years, despite significant differences in both reaction and transport timescales (Figure 9). Finally, while NO_3^- concentration measurements cannot detect these coupled responses, the interannual variability in soil NO_3^- cycling is recorded in NO_3^- isotopes (Figure 10). This is because proportional changes in nitrification and denitrification rates can result in similar soil NO_3^- concentrations, but the relative cycling intensity of these two processes—specifically the fraction of produced NO_3^- removed by denitrification—is directly reflected in NO_3^- isotopes (Casciotti, 2016).

4.2.3. Parsimonious Models as Learning Platforms

We should note that the seasonal variability of NO_3^- sources and the dependence of denitrification on soil moisture conditions have been extensively studied in biogeochemical literature, so we claim no originality for this mechanism. However, it is remarkable that such patterns can be discerned by a relatively simple model at the scale of a mesoscale watershed. This provides a compelling proof-of-concept that models explicitly incorporating water age distributions can effectively capture key features of watershed-scale NO_3^- reactive transport. The findings also reinforce the functional homogeneity of intensively managed agricultural watersheds in the U.S. Upper Midwest, which allows their behavior to be reproduced using parsimonious models with high potential for transferability. In doing so, we extend the conclusions of Basu, Rao, et al. (2010), demonstrating that such models are effective not only for simulating hydrograph responses but also for representing fundamental biogeochemical processes in these highly engineered systems.

Like any modeling approach, the simple model used in this study has inherent limitations. Most notably, the assumption of interannually constant C_{lim} values limits the model's predictive capability beyond the study period. Additionally, its spatially lumped formulation restricts its utility to providing top-down constraints on dominant processes inferred from watershed-scale observations. In this context, the model serves as a fit-for-purpose benchmark that explicitly accounts for water age distributions and leverages NO_3^- isotopic fingerprinting to evaluate key biogeochemical controls on NO_3^- export (i.e., seasonally variable C_{lim} and wetness-dependent denitrification). Assuming that water mixing is adequately represented in this benchmark, residuals between modeled and observed NO_3^- concentrations and isotopes offer direct insights into the validity of the hypothesized processes. For example, during the unusually wet fall and winter of 2022, observed NO_3^- concentrations were higher and NO_3^- isotope values lower than predicted (Figures 8c and 8g), suggesting that soil mineralization and nitrification increased at a rate that outpaced the denitrification response. In the following spring, continued wet

19447973, 2025, 10, Downloaded from https://agupubs.onlinelibrary.wiley.com/doi/10.1029/2024WR039718 by Readcube (Labtiva Inc.), Wiley Online Library on [28/10/2025]. See the Terms and Conditions (https://onlinelibrary.wiley.com/terms-and-conditions) on Wiley Online Library for rules of use; OA articles are governed by the applicable Creative Commons License

conditions may have enhanced denitrification more strongly than the model predicted, leading to decreased NO_3^- concentrations, elevated $\delta^{18}O$ values, and an underestimation of the annual LWMV of $\delta^{18}O$ by the model (Figures 8c–8h). Future benchmarking efforts should explore alternative representations of NO_3^- source zone dynamics and denitrification (e.g., accounting for delayed onset due to O_2 inhibition) to more fully characterize the complexity and variability of watershed-scale N reactive transport.

To predict how watershed N cycling and N export may respond to future climate and land use changes, spatially distributed, process-based watershed biogeochemical models are commonly used. The biogeochemical components of these models are typically based on reaction rate laws and kinetic terms determined under well-controlled and well-mixed laboratory conditions. However, due to the lack of data at appropriate scales, as well as the high dimensionality of model parameter space, scaling up these small-scale biogeochemical mechanisms to complex, heterogeneous watershed systems is often difficult to justify (Li et al., 2021). Additionally, a disconnect persists between widely used hydrological and biogeochemical models in representing the distinct roles of celerity and pore-scale flow velocity in shaping hydrograph responses and solute transport at the watershed scale (Hrachowitz et al., 2016; Ilampooranan et al., 2019). We conclude that integrating water age modeling and NO_3^- isotopic analysis in a parsimonious modeling framework can reveal and reconcile the macroscale mechanisms governing watershed functions. The combined use of these powerful tools with distributed models may prove effective in gaining a more holistic understanding of how watershed N cycling and export respond to changing climate and environmental conditions.

4.3. Implications for N Legacy Effects and NO_3^- Loss Reduction

It is increasingly recognized that legacy N is a major contributor to watershed NO_3^- export, leading to lag times between the implementation of conservation measures and measurable improvements in water quality (Basu et al., 2022). Although decade-long legacy effects have been documented for large river basins (Van Meter et al., 2018), it remains poorly quantified how NO_3^- export are influenced by both hydrologic and biogeochemical N legacy effects in intensively tile-drained mesoscale watersheds across the U.S. Upper Midwest, where the highest riverine NO_3^- yields have been reported (David et al., 2010). By linking N surplus and NO_3^- export across 478 U.S. watersheds, recent work by Van Meter et al. (2023) demonstrated that long-term NO_3^- FWMC tends to respond more linearly to N surplus in watersheds influenced by tile drainage. This contrasts with non-tile-drained agricultural watersheds, where widespread hysteresis in the N surplus-export relationship indicates substantial legacy N accumulation. In the UER, the long-term relationship between NO_3^- FWMC and N surplus is similarly non-hysteretic (Figure S2c in Supporting Information S1). However, the absence of a significant linear relationship between them suggests that NO_3^- export is co-regulated by competing hydrologic and biogeochemical factors that go behind the simple control of N surplus inputs.

Under the framework of the Damökhler number, a strong hydrologic legacy effect is characterized by long timescales for both water transit times and denitrification. In this study, both estimated median age (Figures 7c and 7d) and RT_{50} (Figures 9c and 9d) are subject to uncertainties, resulting in a relatively wide range for the estimated flow-weighted mean Da_{50} (i.e., 0.2 to 2) (Figure 9f). However, the upper bound of our estimated mean median age over the 30-year period (i.e., 399 days) is well within the reported range of 90–650 days for various lowland and sloping watersheds in temperate climates (Benettin et al., 2017; Harman, 2015; Klaus et al., 2015; Rodriguez et al., 2018; Soulsby et al., 2015; van der Velde et al., 2012). It is also significantly higher than the mean median age of about 100 days estimated for tile drainage using a similar SAS modeling framework (Yu et al., 2023). Therefore, using this upper bound as a conservative estimate suggests that about half of the annual precipitation would exit the watershed within a year. Similarly, considering the lower bound of the estimated mean actual denitrification rate (i.e., 0.001 $days^{-1}$), NO_3^- in a water parcel would decay exponentially to about 10% of its initial concentration in 5 years. While contributions from old water would persist due to the long tails of water age distributions, the impact of old water on NO_3^- export is expected to diminish rapidly within 5 years. Together, these back-of-the-envelope calculations depict a high flow-through, reactive system that should not experience decade-long hydrologic legacy effects. This analysis also illuminates that, despite substantial landscape modification, intensively tile-drained Midwestern watersheds can function as both active transporters and transformers of N. The relative importance of these roles is largely governed by their dynamic responses to changing wetness conditions.

19447973, 2025, 10, Downloaded from https://agupubs.onlinelibrary.wiley.com/doi/10.1029/2024WR039718 by Readcube (Labtiva Inc.), Wiley Online Library on [28/10/2025]. See the Terms and Conditions (https://onlinelibrary.wiley.com/terms-and-conditions) on Wiley Online Library for rules of use; OA articles are governed by the applicable Creative Commons License

On the other hand, our results also reveal a strong buffering capacity in NO_3^- source production and mobilization (Section 4.2.2), which can be interpreted as a manifestation of biogeochemical legacy effects. This buffering may dampen the sensitivity of NO_3^- export to variations in N inputs, helping to explain the absence of a linear relationship between long-term NO_3^- FWMC and N surplus (Figure S2c in Supporting Information S1). This interpretation is further supported by our NO_3^- isotopic analysis, which shows that watershed NO_3^- export was sustained by an apparently homogeneous source with a consistent isotopic signature (Figure 4), implying the accumulation of a labile N pool resulting from long-term inputs via fertilizer application and biological N fixation.

Importantly, the majority of NO_3^- export in the UER can be attributed to the convergence of high soil NO_3^- accumulation and the activation of tile drainage during the winter-spring season. Thus, conservation practices that can increase N retention through microbial or plant assimilation during this period may help stabilize the soil organic N pool and mitigate the expression of biogeochemical legacy effects. In a corn-soybean field with productive Mollisol soil near the UER, Gentry et al. (2024) showed that combining non-leguminous winter cover crops with a change in fertilizer timing from fall to just before corn planting—thereby avoiding N accumulation over the winter-spring season—reduced tile drainage NO_3^- loads by 40% over a 4-year period. Similarly, Smith et al. (2013) demonstrated that converting conventional corn-soybean systems to perennial biofuel crops on organic N-rich Mollisols nearly eliminated tile drainage NO_3^- yields within 4 years. When viewed alongside with the minor hydrologic legacy effect revealed in this study, these results suggest that large-scale changes in management practices or cropping systems have the potential to significantly reduce NO_3^- loads from intensively tile-drained watersheds within a relatively short timeframe.

5. Conclusions

While both seasonally variable NO_3^- export regimes and interannual NO_3^- chemostasis have been widely observed and studied in intensively managed agricultural watersheds, this study is, to our knowledge, the first to combine SAS functions and NO_3^- isotopes to explore the underlying mechanisms driving these emergent C-Q relationships. This was achieved by integrating the C-Q relationships with the dynamics of water age and NO_3^- isotopes, and by conceptualizing watershed-scale NO_3^- reactive transport using a simple transit time-based and isotope-aided transport model. Key findings from these analyses are summarized below.

1. Composite SAS-based water age modeling revealed a pronounced inverse storage effect and strong young water preference under high-flow conditions, emphasizing the role of fluctuating groundwater depths and tile drain activation in controlling water mixing.
2. During dry periods, activation of shallower flow and NO_3^- sources produces a NO_3^-flushing response, while tile drain activation and enhanced soil-stream connectivity via soil preferential flow lead to chemostatic NO_3^- export under high-flow conditions.
3. The parsimonious modeling approach identified a strong seasonal pattern in NO_3^- source availability and a wetness dependence for denitrification, providing strong evidence that NO_3^- chemostasis at the interannual scale is driven by coupled and proportional responses of soil NO_3^- production, denitrification, and flow path activation to changing wetness conditions.
4. Although some uncertainty remains, estimated transport and reaction timescales suggest minor hydrologic N legacy effects in the UER. However, substantial N stocks in fertile Mollisols can impose strong biogeochemical legacy effects by sustaining NO_3^- source production and mobilization over time.
5. Intensively tile-drained agricultural watersheds in the U.S. Upper Midwest can function as both N transporters and transformers. Large-scale interventions that reduce soil NO_3^- availability during winter and spring have the potential to significantly reduce NO_3^- export within a relatively short timeframe.
6. Integrating SAS functions and NO_3^- isotopes through coupled tracer measurement and mechanistic modeling holds strong promise for uncovering macroscale controls on watershed-scale N reactive transport.

Conflict of Interest

The authors declare no conflicts of interest relevant to this study.

Data Availability Statement

The trans-SAS model code used for water age modeling is obtained from Benettin and Bertuzzo (2018b). Limited modifications and numerical operations of the trans-SAS model code are fully described in Section 2.3 and Text S2 in Supporting Information S1 of this paper. The water age-based NO_3^- isotopologue model used for NO_3^- transport modeling is adapted from Yu et al. (2023) and is available at Yu (2023). The modifications to this transport model are fully described in Section 2.4 of this paper. The input climate, hydrological, and tracer data for running the SAS and NO_3^- models, as well as the model output for reproducing the presented results, are available at Sha and Yu (2024).

Acknowledgments
This work was funded by USDA-NIFA Hatch grant ILLU-875-983 and NSF Award 2442450. Sha is supported by an Illinois Distinguished Fellowship. We thank Carlos Guacho, Annette Vasquez, Nora Danaher, and Courtney Hau for their assistance with field sampling and laboratory analyses.

References

Aubert, A. H., Kirchner, J. W., Gascuel-Odoux, C., Faucheux, M., Gruau, G., & Mérot, P. (2014). Fractal water quality fluctuations spanning the periodic table in an intensively farmed watershed. *Environmental Science & Technology*, *48*(2), 930–937. https://doi.org/10.1021/es403723r

Basu, N. B., Destouni, G., Jawitz, J. W., Thompson, S. E., Loukinova, N. V., Darracq, A., et al. (2010). Nutrient loads exported from managed catchments reveal emergent biogeochemical stationarity. *Geophysical Research Letters*, *37*(23). https://doi.org/10.1029/2010GL045168

Basu, N. B., Rao, P. S. C., Winzeler, H. E., Kumar, S., Owens, P., & Merwade, V. (2010b). Parsimonious modeling of hydrologic responses in engineered watersheds: Structural heterogeneity versus functional homogeneity. *Water Resources Research*, *46*(4). https://doi.org/10.1029/2009WR007803

Basu, N. B., Van Meter, K. J., Byrnes, D. K., Van Cappellen, P., Brouwer, R., Jacobsen, B. H., et al. (2022). Managing nitrogen legacies to accelerate water quality improvement. *Nature Geoscience*, *15*(2), 97–105. https://doi.org/10.1038/s41561-021-00889-9

Batal, A., Dale, N., & Persia, M. (2011). *Ingredient analysis table* (2012 ed.). Feed-stuffs.

Bauwe, A., Kahle, P., Tiemeyer, B., & Lennartz, B. (2020). Hydrology is the key factor for nitrogen export from tile-drained catchments under consistent land-management. *Environmental Research Letters*, *15*(9), 094050. https://doi.org/10.1088/1748-9326/aba580

Benettin, P., & Bertuzzo, E. (2018a). tran-SAS v1. 0: A numerical model to compute catchment-scale hydrologic transport using StorAge Selection functions. *Geoscientific Model Development*, *11*(4), 1627–1639. https://doi.org/10.5194/gmd-11-1627-2018

Benettin, P., & Bertuzzo, E. (2018b). tran-SAS v1.0 [Code]. *Zenodo*. https://doi.org/10.5281/zenodo.1203600

Benettin, P., Fovet, O., & Li, L. (2020). Nitrate removal and young stream water fractions at the catchment scale. *Hydrological Processes*, *34*(12), 2725–2738. https://doi.org/10.1002/hyp.13781

Benettin, P., Rodriguez, N. B., Sprenger, M., Kim, M., Klaus, J., Harman, C. J., et al. (2022). Transit time estimation in catchments: Recent developments and future directions. *Water Resources Research*, *58*(11), e2022WR033096. https://doi.org/10.1029/2022wr033096

Benettin, P., Soulsby, C., Birkel, C., Tetzlaff, D., Botter, G., & Rinaldo, A. (2017). Using SAS functions and high-resolution isotope data to unravel travel time distributions in headwater catchments. *Water Resources Research*, *53*(3), 1864–1878. https://doi.org/10.1002/2016wr020117

Blann, K. L., Anderson, J. L., Sands, G. R., & Vondracek, B. (2009). Effects of agricultural drainage on aquatic ecosystems: A review. *Critical Reviews in Environmental Science and Technology*, *39*(11), 909–1001. https://doi.org/10.1080/10643380801977966

Borriero, A., Musolff, A., Kumar, R., Fleckenstein, J. H., Lutz, S. R., & Nguyen, T. V. (2024). The value of instream stable water isotope and nitrate concentration data for calibrating a travel time-based water quality model. *Hydrological Processes*, *38*(5), e15154. https://doi.org/10.1002/hyp.15154

Boshers, D. S., Granger, J., Tobias, C. R., Böhlke, J. K., & Smith, R. L. (2019). Constraining the oxygen isotopic composition of nitrate produced by nitrification. *Environmental Science & Technology*, *53*(3), 1206–1216. https://doi.org/10.1021/acs.est.8b03386

Botter, G., Bertuzzo, E., Bellin, A., & Rinaldo, A. (2005). On the Lagrangian formulations of reactive solute transport in the hydrologic response. *Water Resources Research*, *41*(4). https://doi.org/10.1029/2004wr003544

Botter, G., Bertuzzo, E., & Rinaldo, A. (2011). Catchment residence and travel time distributions: The master equation. *Geophysical Research Letters*, *38*(11). https://doi.org/10.1029/2011gl047666

Botter, G., Daly, E., Porporato, A., Rodriguez-Iturbe, I., & Rinaldo, A. (2008). Probabilistic dynamics of soil nitrate: Coupling of ecohydrological and biogeochemical processes. *Water Resources Research*, *44*(3). https://doi.org/10.1029/2007wr006108

Bouwman, L., Goldewijk, K. K., Van Der Hoek, K. W., Beusen, A. H., Van Vuuren, D. P., Willems, J., et al. (2013). Exploring global changes in nitrogen and phosphorus cycles in agriculture induced by livestock production over the 1900–2050 period. *Proceedings of the National Academy of Sciences*, *110*(52), 20882–20887. https://doi.org/10.1073/pnas.1012878108

Brauer, C. C., Teuling, A. J., Torfs, P. J. J. F., & Uijlenhoet, R. (2013). Investigating storage-discharge relations in a lowland catchment using hydrograph fitting, recession analysis, and soil moisture data. *Water Resources Research*, *49*(7), 4257–4264. https://doi.org/10.1002/wrcr.20320

Brauer, C. C., Teuling, A. J., Torfs, P. J. J. F., & Uijlenhoet, R. (2014). The Wageningen lowland runoff simulator (WALRUS): A lumped rainfall–runoff model for catchments with shallow groundwater. *Geoscientific Model Development*, *7*(5), 2313–2332. https://doi.org/10.5194/gmd-7-2313-2014

Byrnes, D. K., Van Meter, K. J., & Basu, N. B. (2020). Long-term shifts in US nitrogen sources and sinks revealed by the new TREND-nitrogen data set (1930–2017). *Global Biogeochemical Cycles*, *34*(9), e2020GB006626. https://doi.org/10.1029/2020gb006626

Cain, M. R., Woo, D. K., Kumar, P., Keefer, L., & Ward, A. S. (2022). Antecedent conditions control thresholds of tile-runoff generation and nitrogen export in intensively managed landscapes. *Water Resources Research*, *58*(2), e2021WR030507. https://doi.org/10.1029/2021WR030507

Casciotti, K. L. (2016). Nitrogen and oxygen isotopic studies of the marine nitrogen cycle. *Annual Review of Marine Science*, *8*(1), 379–407. https://doi.org/10.1146/annurev-marine-010213-135052

Danalatos, G. J., Wolter, C., Archontoulis, S. V., & Castellano, M. J. (2022). Nitrate losses across 29 Iowa watersheds: Measuring long-term trends in the context of interannual variability. *Journal of Environmental Quality*, *51*(4), 708–718. https://doi.org/10.1002/jeq2.20349

David, M. B., Drinkwater, L. E., & McIsaac, G. F. (2010). Sources of nitrate yields in the Mississippi river basin. *Journal of Environmental Quality*, *39*(5), 1657–1667. https://doi.org/10.2134/jeq2010.0115

19447973, 2025, 10, Downloaded from https://agupubs.onlinelibrary.wiley.com/doi/10.1029/2024WR039718 by Readcube (Labtiva Inc.), Wiley Online Library on [28/10/2025]. See the Terms and Conditions (https://onlinelibrary.wiley.com/terms-and-conditions) on Wiley Online Library for rules of use; OA articles are governed by the applicable Creative Commons License

David, M. B., Gentry, L. E., Kovacic, D. A., & Smith, K. M. (1997). Nitrogen balance in and export from an agricultural watershed. *American Society of Agronomy, Crop Science Society of America, and Soil Science Society of America*, *26*(4), 1038–1048. https://doi.org/10.2134/jeq1997.00472425002600040015x

David, M. B., Mitchell, C. A., Gentry, L. E., & Salemme, R. K. (2016). Chloride sources and losses in two tile-drained agricultural watersheds. *Journal of Environmental Quality*, *45*(1), 341–348. https://doi.org/10.2134/jeq2015.06.0302

Davidson, E. A., & Janssens, I. A. (2006). Temperature sensitivity of soil carbon decomposition and feedbacks to climate change. *Nature*, *440*(7081), 165–173. https://doi.org/10.1038/nature04514

Denk, T. R., Mohn, J., Decock, C., Lewicka-Szczebak, D., Harris, E., Butterbach-Bahl, K., et al. (2017). The nitrogen cycle: A review of isotope effects and isotope modeling approaches. *Soil Biology and Biochemistry*, *105*, 121–137. https://doi.org/10.1016/j.soilbio.2016.11.015

Druhan, J. L., & Maher, K. (2017). The influence of mixing on stable isotope ratios in porous media: A revised Rayleigh model. *Water Resources Research*, *53*(2), 1101–1124. https://doi.org/10.1002/2016wr019666

Fang, Y., Koba, K., Makabe, A., Takahashi, C., Zhu, W., Hayashi, T., et al. (2015). Microbial denitrification dominates nitrate losses from forest ecosystems. *Proceedings of the National Academy of Sciences*, *112*(5), 1470–1474. https://doi.org/10.1073/pnas.1416776112

Fehrenbacher, J. B. (1984). Soils of Illinois. *Bulletin (University of Illinois at Urbana-Champaign. Agricultural Experiment Station)*, *778*.

Fernández, F. G., Fabrizzi, K. P., & Naeve, S. L. (2017). Corn and soybean's season-long in-situ nitrogen mineralization in drained and undrained soils. *Nutrient Cycling in Agroecosystems*, *107*(1), 33–47. https://doi.org/10.1007/s10705-016-9810-1

Gentry, L. E., David, M. B., & McIsaac, G. F. (2014). Variation in riverine nitrate flux and fall nitrogen fertilizer application in east-central Illinois. *Journal of Environmental Quality*, *43*(4), 1467–1474. https://doi.org/10.2134/jeq2013.12.0499

Gentry, L. E., Green, J. M., Mitchell, C. A., Andino, L. F., Rolf, M. K., Schaefer, D., & Nafziger, E. D. (2024). Split fertilizer nitrogen application with a cereal rye cover crop reduces tile nitrate loads in a corn–soybean rotation. *Journal of Environmental Quality*, *53*(1), 90–100. https://doi.org/10.1002/jeq2.20530

Godsey, S. E., Kirchner, J. W., & Clow, D. W. (2009). Concentration–discharge relationships reflect chemostatic characteristics of US catchments. *Hydrological Processes: International Journal*, *23*(13), 1844–1864. https://doi.org/10.1002/hyp.7315

Granger, J., Sigman, D. M., Lehmann, M. F., & Tortell, P. D. (2008). Nitrogen and oxygen isotope fractionation during dissimilatory nitrate reduction by denitrifying bacteria. *Limnology & Oceanography*, *53*(6), 2533–2545. https://doi.org/10.4319/lo.2008.53.6.2533

Granger, J., & Wankel, S. D. (2016). Isotopic overprinting of nitrification on denitrification as a ubiquitous and unifying feature of environmental nitrogen cycling. *Proceedings of the National Academy of Sciences*, *113*(42), E6391–E6400. https://doi.org/10.1073/pnas.1601383113

Green, C. T., Puckett, L. J., Böhlke, J. K., Bekins, B. A., Phillips, S. P., Kauffman, L. J., et al. (2008). Limited occurrence of denitrification in four shallow aquifers in agricultural areas of the United States. *Journal of Environmental Quality*, *37*(3), 994–1009. https://doi.org/10.2134/jeq2006.0419

Groffman, P. M., Butterbach-Bahl, K., Fulweiler, R. W., Gold, A. J., Morse, J. L., Stander, E. K., et al. (2009). Challenges to incorporating spatially and temporally explicit phenomena (hotspots and hot moments) in denitrification models. *Biogeochemistry*, *93*(1–2), 49–77. https://doi.org/10.1007/s10533-008-9277-5

Harman, C. J. (2015). Time-variable transit time distributions and transport: Theory and application to storage-dependent transport of chloride in a watershed. *Water Resources Research*, *51*(1), 1–30. https://doi.org/10.1002/2014wr015707

Hester, E. T., & Fox, G. A. (2020). Preferential flow in riparian groundwater: Gateways for watershed solute transport and implications for water quality management. *Water Resources Research*, *56*(12), e2020WR028186. https://doi.org/10.1029/2020wr028186

Hrachowitz, M., Benettin, P., Van Breukelen, B. M., Fovet, O., Howden, N. J., Ruiz, L., et al. (2016). Transit times—The link between hydrology and water quality at the catchment scale. *Wiley Interdisciplinary Reviews: Water*, *3*(5), 629–657. https://doi.org/10.1002/wat2.1155

Hrachowitz, M., Fovet, O., Ruiz, L., & Savenije, H. H. (2015). Transit time distributions, legacy contamination and variability in biogeochemical 1/fα scaling: How are hydrological response dynamics linked to water quality at the catchment scale? *Hydrological Processes*, *29*(25), 5241–5256. https://doi.org/10.1002/hyp.10546

Hrachowitz, M., Savenije, H., Bogaard, T. A., Tetzlaff, D., & Soulsby, C. (2013). What can flux tracking teach us about water age distribution patterns and their temporal dynamics? *Hydrology and Earth System Sciences*, *17*(2), 533–564. https://doi.org/10.5194/hess-17-533-2013

Hu, Y., Yu, Z., Yang, W. H., Margenot, A. J., Gentry, L. E., Wander, M. M., et al. (2024). Deciphering the isotopic imprint of nitrate to reveal nitrogen source and transport mechanisms in a tile-drained agroecosystem. *Journal of Geophysical Research: Biogeosciences*, *129*(8), e2024JG008027. https://doi.org/10.1029/2024jg008027

Ilampooranan, I., Van Meter, K. J., & Basu, N. B. (2019). A race against time: Modeling time lags in watershed response. *Water Resources Research*, *55*(5), 3941–3959. https://doi.org/10.1029/2018wr023815

Kaandorp, V. P., Broers, H. P., Van Der Velde, Y., Rozemeijer, J., & De Louw, P. G. (2021). Time lags of nitrate, chloride, and tritium in streams assessed by dynamic groundwater flow tracking in a lowland landscape. *Hydrology and Earth System Sciences*, *25*(6), 3691–3711. https://doi.org/10.5194/hess-25-3691-2021

Kendall, C., Elliott, E. M., & Wankel, S. D. (2007). Tracing anthropogenic inputs of nitrogen to ecosystems. *Stable Isotopes in Ecology and Environmental Science*, 375–449. https://doi.org/10.1002/9780470691854.ch12

Kim, M., & Harman, C. J. (2022). Transit times and storage selection functions in idealized hillslopes with steady infiltration. *Water Resources Research*, *58*(5), e2019WR025917. https://doi.org/10.1029/2019wr025917

Kirchner, J. W. (2009). Catchments as simple dynamical systems: Catchment characterization, rainfall-runoff modeling, and doing hydrology backward. *Water Resources Research*, *45*(2). https://doi.org/10.1029/2008wr006912

Klaus, J., Chun, K. P., McGuire, K. J., & McDonnell, J. J. (2015). Temporal dynamics of catchment transit times from stable isotope data. *Water Resources Research*, *51*(6), 4208–4223. https://doi.org/10.1002/2014wr016247

Klaus, J., Zehe, E., Elsner, M., Külls, C., & McDonnell, J. J. (2013). Macropore flow of old water revisited: Experimental insights from a tile-drained hillslope. *Hydrology and Earth System Sciences*, *17*(1), 103–118. https://doi.org/10.5194/hess-17-103-2013

Knapp, J. L., Li, L., & Musolff, A. (2022). Hydrologic connectivity and source heterogeneity control concentration–discharge relationships. *Hydrological Processes*, *36*(9), e14683. https://doi.org/10.1002/hyp.14683

Kolbe, T., de Dreuzy, J. R., Abbott, B. W., Aquilina, L., Babey, T., Green, C. T., et al. (2019). Stratification of reactivity determines nitrate removal in groundwater. *Proceedings of the National Academy of Sciences*, *116*(7), 2494–2499. https://doi.org/10.1073/pnas.1816892116

Kumar, R. D., Heße, F., Rao, P. S. C., Musolff, A., Jawitz, J. W., Sarrazin, F., et al. (2020). Strong hydroclimatic controls on vulnerability to subsurface nitrate contamination across Europe. *Nature Communications*, *11*(1), 6302. https://doi.org/10.1038/s41467-020-19955-8

Leighton, M. M., Ekblaw, G. E., & Horberg, L. (1948). Physiographic divisions of Illinois. *The Journal of Geology*, *56*(1), 16–33. https://doi.org/10.1086/625474

Li, L., Sullivan, P. L., Benettin, P., Cirpka, O. A., Bishop, K., Brantley, S. L., et al. (2021). Toward catchment hydro-biogeochemical theories. *Wiley Interdisciplinary Reviews: Water*, *8*(1), e1495. https://doi.org/10.1002/wat2.1495

19447973, 2025, 10, Downloaded from https://agupubs.onlinelibrary.wiley.com/doi/10.1029/2024WR039718 by Readcube (Labtiva Inc.), Wiley Online Library on [28/10/2025]. See the Terms and Conditions (https://onlinelibrary.wiley.com/terms-and-conditions) on Wiley Online Library for rules of use; OA articles are governed by the applicable Creative Commons License

Loschko, M., Wöhling, T., Rudolph, D. L., & Cirpka, O. A. (2016). Cumulative relative reactivity: A concept for modeling aquifer-scale reactive transport. *Water Resources Research*, *52*(10), 8117–8137. https://doi.org/10.1002/2016wr019080

Ma, Z., Guan, K., Peng, B., Sivapalan, M., Li, L., Pan, M., et al. (2023). Agricultural nitrate export patterns shaped by crop rotation and tile drainage. *Water Research*, *229*, 119468. https://doi.org/10.1016/j.watres.2022.119468

Maharjan, B., Venterea, R. T., & Rosen, C. (2014). Fertilizer and irrigation management effects on nitrous oxide emissions and nitrate leaching. *Agronomy Journal*, *106*(2), 703–714. https://doi.org/10.2134/agronj2013.0179

Marinos, R. E., Van Meter, K. J., & Basu, N. B. (2020). Is the river a chemostat? Scale versus land use controls on nitrate concentration-discharge dynamics in the upper Mississippi river basin. *Geophysical Research Letters*, *47*(16), e2020GL087051. https://doi.org/10.1029/2020gl087051

Mehnert, E., Dey, W. S., Hwang, H. H., Keefer, D. A., Holm, T. R., Johnson, T. M., et al. (2005). Mass Balance of nitrogen and phosphorus in an agricultural watershed: The shallow groundwater component. Open File Series 2005-03.

Moore, E. M., Barclay, J. R., Haynes, A. B., Jackson, K. E., Bisson, A. M., Briggs, M. A., & Helton, A. M. (2023). Where the past meets the present: Connecting nitrogen from watersheds to streams through groundwater flowpaths. *Environmental Research Letters*, *18*(12), 124039. https://doi.org/10.1088/1748-9326/ad0c86

Musolff, A., Schmidt, C., Selle, B., & Fleckenstein, J. H. (2015). Catchment controls on solute export. *Advances in Water Resources*, *86*, 133–146. https://doi.org/10.1016/j.advwatres.2015.09.026

NADP. (2024). National atmospheric deposition program for Bonville, Illinois (site ID IL11). Retrieved from https://www.usgs.gov/mission-areas/water-resources/science/national-atmospheric-deposition-program-nadp

Nguyen, T. V., Kumar, R., Musolff, A., Lutz, S. R., Sarrazin, F., Attinger, S., & Fleckenstein, J. H. (2022). Disparate seasonal nitrate export from nested heterogeneous subcatchments revealed with StorAge Selection functions. *Water Resources Research*, *58*(3), e2021WR030797. https://doi.org/10.1029/2021wr030797

Preza-Fontes, G., Nafziger, E. D., Christianson, L. E., & Pittelkow, C. M. (2020). Relationship of in-season soil nitrogen concentration with corn yield and potential nitrogen losses. *Soil Science Society of America Journal*, *84*(4), 1296–1306. https://doi.org/10.1002/saj2.20117

Redder, B. W., Kennedy, C. D., Buda, A. R., Folmar, G., & Boyer, E. W. (2021). Groundwater contributions of flow and nitrogen in a headwater agricultural watershed. *Hydrological Processes*, *35*(5), e14179. https://doi.org/10.1002/hyp.14179

Rhoads, B. L., Lewis, Q. W., & Andresen, W. (2016). Historical changes in channel network extent and channel planform in an intensively managed landscape: Natural versus human-induced effects. *Geomorphology*, *252*, 17–31. https://doi.org/10.1016/j.geomorph.2015.04.021

Rinaldo, A., Benettin, P., Harman, C. J., Hrachowitz, M., McGuire, K. J., Van Der Velde, Y., et al. (2015). Storage selection functions: A coherent framework for quantifying how catchments store and release water and solutes. *Water Resources Research*, *51*(6), 4840–4847. https://doi.org/10.1002/2015wr017273

Rinaldo, A., Botter, G., Bertuzzo, E., Uccelli, A., Settin, T., & Marani, M. (2006). Transport at basin scales: 1. Theoretical framework. *Hydrology and Earth System Sciences*, *10*(1), 19–29. https://doi.org/10.5194/hess-10-19-2006

Rodriguez, N. B., & Klaus, J. (2019). Catchment travel times from composite storage selection functions representing the superposition of streamflow generation processes. *Water Resources Research*, *55*(11), 9292–9314. https://doi.org/10.1029/2019wr024973

Rodriguez, N. B., McGuire, K. J., & Klaus, J. (2018). Time-varying storage–water age relationships in a catchment with a mediterranean climate. *Water Resources Research*, *54*(6), 3988–4008. https://doi.org/10.1029/2017wr021964

Rozemeijer, J. C., Van Der Velde, Y., McLaren, R. G., Van Geer, F. C., Broers, H. P., & Bierkens, M. F. P. (2010). Integrated modeling of groundwater–surface water interactions in a tile-drained agricultural field: The importance of directly measured flow route contributions. *Water Resources Research*, *46*(11). https://doi.org/10.1029/2010wr009155

Schulte-Uebbing, L. F., Beusen, A. H., Bouwman, A. F., & De Vries, W. (2022). From planetary to regional boundaries for agricultural nitrogen pollution. *Nature*, *610*(7932), 507–512. https://doi.org/10.1038/s41586-022-05158-2

Seibert, J., Grabs, T., Köhler, S., Laudon, H., Winterdahl, M., & Bishop, K. (2009). Linking soil-and stream-water chemistry based on a riparian flow-concentration integration model. *Hydrology and Earth System Sciences*, *13*(12), 2287–2297. https://doi.org/10.5194/hess-13-2287-2009

Sha, M., & Yu, Z. (2024). Coupled hydrologic and biogeochemical responses of nitrate export in a tile-drained agricultural watershed revealed by SAS functions and nitrate isotopes [Dataset]. *Zenodo*. https://doi.org/10.5281/zenodo.14497901

Smith, C. M., David, M. B., Mitchell, C. A., Masters, M. D., Anderson-Teixeira, K. J., Bernacchi, C. J., & DeLucia, E. H. (2013). Reduced nitrogen losses after conversion of row crop agriculture to perennial biofuel crops. *Journal of Environmental Quality*, *42*(1), 219–228. https://doi.org/10.2134/jeq2012.0210

Soller, D. R., Price, S. D., Kempton, J. P., & Berg, R. C. (1999). Three-dimensional geologic maps of Quaternary sediments in east-central Illinois. *The Survey*.

Soulsby, C., Birkel, C., Geris, J., Dick, J., Tunaley, C., & Tetzlaff, D. (2015). Stream water age distributions controlled by storage dynamics and nonlinear hydrologic connectivity: Modeling with high-resolution isotope data. *Water Resources Research*, *51*(9), 7759–7776. https://doi.org/10.1002/2015wr017888

Thompson, S. E., Basu, N. B., Lascurain Jr, J., Aubeneau, A., & Rao, P. S. C. (2011). Relative dominance of hydrologic versus biogeochemical factors on solute export across impact gradients. *Water Resources Research*, *47*(10). https://doi.org/10.1029/2010wr009605

Urban, M. A., & Rhoads, B. L. (2003). Catastrophic human-induced change in stream-channel planform and geometry in an agricultural watershed, Illinois, USA. *Annals of the Association of American Geographers*, *93*(4), 783–796. https://doi.org/10.1111/j.1467-8306.2003.09304001.x

USDA-NRCS. (2016). Gridded soil survey geographic (gSSURGO) database for Douglas County, Illinois. Retrieved from https://gdg.sc.egov.usda.gov/

Valayamkunnath, P., Barlage, M., Chen, F., Gochis, D. J., & Franz, K. J. (2020). Mapping of 30-meter resolution tile-drained croplands using a geospatial modeling approach. *Scientific Data*, *7*(1), 257. https://doi.org/10.1038/s41597-020-00596-x

Van der Velde, Y., De Rooij, G. H., Rozemeijer, J. C., Van Geer, F. C., & Broers, H. P. (2010). Nitrate response of a lowland catchment: On the relation between stream concentration and travel time distribution dynamics. *Water Resources Research*, *46*(11). https://doi.org/10.1029/2010wr009105

Van Der Velde, Y., Torfs, P. J. J. F., Van Der Zee, S. E. A. T. M., & Uijlenhoet, R. (2012). Quantifying catchment-scale mixing and its effect on time-varying travel time distributions. *Water Resources Research*, *48*(6). https://doi.org/10.1029/2011wr011310

van Meerveld, H. I., Kirchner, J. W., Vis, M. J., Assendelft, R. S., & Seibert, J. (2019). Expansion and contraction of the flowing stream network alter hillslope flowpath lengths and the shape of the travel time distribution. *Hydrology and Earth System Sciences*, *23*(11), 4825–4834. https://doi.org/10.5194/hess-23-4825-2019

Van Meter, K. J., Byrnes, D. K., & Basu, N. B. (2023). Memory and management: Competing controls on long-term nitrate trajectories in US rivers. *Global Biogeochemical Cycles*, *37*(4), e2022GB007651. https://doi.org/10.1029/2022gb007651

19447973, 2025, 10, Downloaded from https://agupubs.onlinelibrary.wiley.com/doi/10.1029/2024WR039718 by Readcube (Labtiva Inc.), Wiley Online Library on [28/10/2025]. See the Terms and Conditions (https://onlinelibrary.wiley.com/terms-and-conditions) on Wiley Online Library for rules of use; OA articles are governed by the applicable Creative Commons License

Van Meter, K. J., Van Cappellen, P., & Basu, N. B. (2018). Legacy nitrogen may prevent achievement of water quality goals in the Gulf of Mexico. *Science*, *360*(6387), 427–430. https://doi.org/10.1126/science.aar4462

Vidon, P., & Cuadra, P. E. (2010). Impact of precipitation characteristics on soil hydrology in tile-drained landscapes. *Hydrological Processes*, *24*(13), 1821–1833. https://doi.org/10.1002/hyp.7627

Vrugt, J. A., & Robinson, B. A. (2007). Improved evolutionary optimization from genetically adaptive multimethod search. *Proceedings of the National Academy of Sciences*, *104*(3), 708–711. https://doi.org/10.1073/pnas.0610471104

Weigand, M. A., Foriel, J., Barnett, B., Oleynik, S., & Sigman, D. M. (2016). Updates to instrumentation and protocols for isotopic analysis of nitrate by the denitrifier method. *Rapid Communications in Mass Spectrometry*, *30*(12), 1365–1383. https://doi.org/10.1002/rcm.7570

Williams, M. R., King, K. W., Ford, W., Buda, A. R., & Kennedy, C. D. (2016). Effect of tillage on macropore flow and phosphorus transport to tile drains. *Water Resources Research*, *52*(4), 2868–2882. https://doi.org/10.1002/2015wr017650

Williams, M. R., King, K. W., Macrae, M. L., Ford, W., Van Esbroeck, C., Brunke, R. I., et al. (2015). Uncertainty in nutrient loads from tile-drained landscapes: Effect of sampling frequency, calculation algorithm, and compositing strategy. *Journal of Hydrology*, *530*, 306–316. https://doi.org/10.1016/j.jhydrol.2015.09.060

Yang, J., Heidbüchel, I., Musolff, A., Reinstorf, F., & Fleckenstein, J. H. (2018). Exploring the dynamics of transit times and subsurface mixing in a small agricultural catchment. *Water Resources Research*, *54*(3), 2317–2335. https://doi.org/10.1002/2017wr021896

Yu, Z. (2023). Linking water age, nitrate export regime, and nitrate isotope biogeochemistry in a tile-drained agricultural field: The nitrate isotopologue transport model [Code]. *Zenodo*. https://doi.org/10.5281/zenodo.7761585

Yu, Z., Hu, Y., Gentry, L. E., Yang, W. H., Margenot, A. J., Guan, K., et al. (2023). Linking water age, nitrate export regime, and nitrate isotope biogeochemistry in a tile-drained agricultural field. *Water Resources Research*, *59*(12), e2023WR034948. https://doi.org/10.1029/2023wr034948

Zhi, W., & Li, L. (2020). The shallow and deep hypothesis: Subsurface vertical chemical contrasts shape nitrate export patterns from different land uses. *Environmental Science & Technology*, *54*(19), 11915–11928. https://doi.org/10.1021/acs.est.0c01340

Zimmer, M. A., & McGlynn, B. L. (2018). Lateral, vertical, and longitudinal source area connectivity drive runoff and carbon export across watershed scales. *Water Resources Research*, *54*(3), 1576–1598. https://doi.org/10.1002/2017wr021718

Zimmer, M. A., Pellerin, B., Burns, D. A., & Petrochenkov, G. (2019). Temporal variability in nitrate-discharge relationships in large rivers as revealed by high-frequency data. *Water Resources Research*, *55*(2), 973–989. https://doi.org/10.1029/2018wr023478

References From the Supporting Information

Allen, R. G., Pereira, L. S., Smith, M., Raes, D., & Wright, J. L. (2005). FAO-56 dual crop coefficient method for estimating evaporation from soil and application extensions. *Journal of Irrigation and Drainage Engineering*, *131*(1), 2–13. https://doi.org/10.1061/(asce)0733-9437(2005)131:1(2)

Asadollahi, M., Stumpp, C., Rinaldo, A., & Benettin, P. (2020). Transport and water age dynamics in soils: A comparative study of spatially integrated and spatially explicit models. *Water Resources Research*, *56*(3), e2019WR025539. https://doi.org/10.1029/2019wr025539

Benettin, P., Rinaldo, A., & Botter, G. (2013). Kinematics of age mixing in advection-dispersion models. *Water Resources Research*, *49*(12), 8539–8551. https://doi.org/10.1002/2013wr014708

Fenicia, F., Kavetski, D., Savenije, H. H., & Pfister, L. (2016). From spatially variable streamflow to distributed hydrological models: Analysis of key modeling decisions. *Water Resources Research*, *52*(2), 954–989. https://doi.org/10.1002/2015wr017398

Illinois Department of Agriculture. (2023). Fertilizer tonnage reports. Retrieved from https://agr.illinois.gov/plants/fertilizer/fertilizer-reports.html

Kaandorp, V. P., De Louw, P. G. B., Van der Velde, Y., & Broers, H. P. (2018). Transient groundwater travel time distributions and age-ranked storage-discharge relationships of three lowland catchments. *Water Resources Research*, *54*(7), 4519–4536. https://doi.org/10.1029/2017wr022461

Kim, M., Volkmann, T. H., Wang, Y., Meira Neto, A. A., Matos, K., Harman, C. J., & Troch, P. A. (2022). Direct observation of hillslope scale StorAge selection functions in experimental hydrologic systems: Geomorphologic structure and preferential discharge of old water. *Water Resources Research*, *58*(3), e2020WR028959. https://doi.org/10.1029/2020wr028959

Knoben, W. J., Freer, J. E., Fowler, K. J., Peel, M. C., & Woods, R. A. (2019). Modular assessment of rainfall–runoff models toolbox (MARRMoT) v1. 2: An open-source, extendable framework providing implementations of 46 conceptual hydrologic models as continuous state-space formulations. *Geoscientific Model Development*, *12*(6), 2463–2480. https://doi.org/10.5194/gmd-12-2463-2019

Teuling, A. J., Lehner, I., Kirchner, J. W., & Seneviratne, S. I. (2010). Catchments as simple dynamical systems: Experience from a Swiss prealpine catchment. *Water Resources Research*, *46*(10). https://doi.org/10.1029/2009wr008777

Wilusz, D. C., Harman, C. J., Ball, W. P., Maxwell, R. M., & Buda, A. R. (2020). Using particle tracking to understand flow paths, age distributions, and the paradoxical origins of the inverse storage effect in an experimental catchment. *Water Resources Research*, *56*(4), e2019WR025140. https://doi.org/10.1029/2019wr025140

19447973, 2025, 10, Downloaded from https://agupubs.onlinelibrary.wiley.com/doi/10.1029/2024WR039718 by Readcube (Labtiva Inc.), Wiley Online Library on [28/10/2025]. See the Terms and Conditions (https://onlinelibrary.wiley.com/terms-and-conditions) on Wiley Online Library for rules of use; OA articles are governed by the applicable Creative Commons License